Structure and properties of small sodium clusters

Ilia A. Solov'yov*
St. Petersburg State Technical University, Politechnicheskaya 29, 195251 St. Petersburg, Russia

Andrey V. Solov'yov† and Walter Greiner
Institut für Theoretische Physik der Universität Frankfurt am Main, Robert-Mayer Straße 8-10, D-60054 Frankfurt am Main, Germany 60054

(Received 16 December 2001; published 29 April 2002)

We have investigated the structure and properties of small metal clusters using all-electron *ab initio* theoretical methods based on the Hartree-Fock approximation, density functional theory, and perturbation theory and compared the results of our calculations with the available experimental data and the results of other theoretical work. We have systematically calculated the optimized geometries of neutral and singly charged sodium clusters having up to 20 atoms, their multipole moments (dipole and quadrupole), static polarizabilities, binding energies per atom, ionization potentials, and frequencies of normal vibration modes. Our calculations demonstrate the important role of many-electron correlations in the formation of the electronic and ionic structure of small metal clusters and form a good basis for further detailed study of their dynamic properties, as well as the structure and properties of other atomic cluster systems.

DOI: 10.1103/PhysRevA.65.053203 PACS number(s): 36.40.−c, 31.15.Ar

I. INTRODUCTION

Atomic clusters and small nanoparticles have been recognized as distinct physical objects with their own properties relatively recently. This became clear after such experimental successes as the discovery of electron shell structure in metal clusters [1], observation of plasmon resonances in metal clusters [2–4] and fullerenes [5,6], formation of singly and doubly charged negative cluster ions [7], and many more. The interest in cluster physics is also closely connected with the fact that cluster properties explain the transition from single atoms or molecules to the solid state. A comprehensive survey of the field can be found in review papers and books; see, e.g., [8–14].

There are many different types of cluster, such as metallic clusters, fullerenes, molecular clusters, semiconductor clusters, organic clusters, quantum dots, and positively and negatively charged clusters, which all have their own features and properties. In this paper we focus on a detailed systematic study of the structure and properties of small metal clusters and in particular sodium clusters using *ab initio* all-electron many-body theory methods.

So far, systematic calculations of sodium cluster properties on the same level of theory as in our present work (i.e., all-electron *ab initio* calculations) have been performed only for clusters with $N \leqslant 10$ [13,15–19], where N is the number of atoms in a cluster. In our work we extend this limit up to $N \leqslant 20$. Note that most of the cited papers are focused on the investigation of neutral cluster properties rather than ions. In our present work we perform a systematic comparative analysis of the properties of neutral and singly charged sodium clusters in the specified size range.

During the last decade, numerous experimental and theoretical investigations of the properties of small metal clusters were performed, as well as of processes involving them. Here we are not able to review even all the essential results obtained in the field and only refer to those that are related most closely to the subject of our paper. In [1], it was experimentally proved that metal clusters have the shell electronic structure, and the magic cluster numbers have been determined by observation of sodium cluster abundances in mass spectra. Experimental studies of the electronic structure and properties of small metal clusters are reported in [20,21] (for reviews, see also [8,10,11,13,14]). In [20], the ionization potentials for a sequence of small neutral and positively charged sodium metal clusters were measured, which independently proved their shell structure. The dipole polarizabilities of sodium clusters were experimentally determined in [21]. The dissociation energies of neutral and positively charged small sodium and potassium metal clusters were measured in [22–24]. The dynamical properties of clusters have been studied by means of photon, electron, and ion scattering. These methods are the traditional tools for probing the properties and internal structure of various physical objects. Using these methods, for example, plasmon excitations in metal clusters [2,25] and fullerenes [6] have been observed (for reviews, see also [8,10]).

Metal clusters have also been studied theoretically. The structural properties of small metal clusters have been widely investigated using quantum chemistry methods. Here we refer to the papers [15–18,26–29], in which optimized geometries, binding energies, ionization potentials, electron structure, and electron transport properties of small lithium and sodium clusters have been calculated. In these papers the systematic analysis of the cluster properties was limited to cluster sizes $N \leqslant 10$. In the present paper we extend this limit up to $N \leqslant 20$ and perform a systematic analysis of various

*Email address: solovyov@rpro.ioffe.rssi.ru

†Permanent address: A. F. Ioffe Physical-Technical Institute of the Russian Academy of Sciences, Politechnicheskaya 26, St. Petersburg, Russia 194021. Email address: solovyov@th.physik.uni-frankfurt.de

cluster characteristics for both neutral clusters and singly charged cluster ions.

In the last few years, a number of papers have been devoted to calculation of the dipole static polarizabilities of neutral sodium and lithium clusters [19,30–33]. Note that most of these studies were performed within the cluster size range $N \leqslant 20$. The results of different theoretical approaches were compared with the experimental data from [21]. However, only in [19], were calculations of the cluster geometries and polarizabilities performed on the same level of theory (i.e., all-electron *ab initio* calculations) as in our work and they were limited to $N \leqslant 8$.

Alternatively, the jellium model for metal clusters has been suggested. This model explains well enough the shell structure of metal clusters and their essential dynamic properties, such as plasmon excitations. Initially, jellium calculations for metal clusters were based on the density functional formalism with the use of pseudopotentials for the description of electron relaxation effects and lattice structure [34]. Fully self-consistent calculations for spherical jellium metal clusters have been performed within the framework of the spin-density-functional method [35] and the Kohn-Sham formalism for the self-consistent determination of electron wave functions [36,37]. The Hartree-Fock scheme for self-consistent determination of the electron wave functions of spherical jellium metal clusters was introduced later in [38,39]. This approach was generalized for axially deformed cluster systems in [40]. The dynamical jellium model for metal clusters, which treats simultaneously the collective vibrational modes (volume vibrations, i.e., breathing, plus shape vibrations) of the ionic jellium background in a cluster, quantized electron motion, and interaction between the electronic and ionic subsystems, was developed in [41,42].

The jellium model provides a very useful basis for studying various collision processes, such as photoabsorption [43], photoionization [5,44,45], elastic [46,47] and inelastic scattering [47–50], electron attachment [51,52], photon emission [53,54] and others, involving metal clusters. On the basis of the jellium model one can develop *ab initio* many-body theories, such as the random phase approximation with exchange or the Dyson equation method, and effectively solve a many-electron correlation problem even for relatatively large cluster systems containing up to 100 atoms or even more. One can find a review of these methods in their application to the electron scattering of metal clusters in [55]. As elucidated in the papers cited above, many-electron correlations are essential for the correct description of various characteristics of cluster systems.

In spite of the fact that the jellium model with all its modifications is rather successful in explaining numerous phenomena involving metal clusters, it obviously has its limits, because this model does not take into account the detailed ionic structure of clusters. The correspondence between predictions of the jellium model and the results of more advanced quantum chemistry calculations has not been examined in a systematic way so far. Partially, this is connected to the fact that quantum chemistry calculations are usually limited to small sizes of clusters, while the jellium model becomes adequate for larger cluster systems. Knowledge of the ranges of applicability of the jellium model and the level of its accuracy is important, because the jellium model often gives a much more efficient theoretical basis, particularly when dealing with larger cluster systems.

In this paper we have undertaken a detailed systematic theoretical study of the structure and properties of sodium clusters beyond the jellium model using all-electron *ab initio* theoretical methods based on the Hartree-Fock approximation, density functional theory, and perturbation theory, for clusters whose size is large enough for jellium calculations. That is, we have calculated optimized geometries of neutral and singly charged sodium clusters consisting of up to 20 atoms, their multipole moments (dipole and quadrupole), static polarizabilities, binding energies per atom, ionization potentials, and frequencies of normal vibration modes. We compare the results of our calculations with the available experimental data and with results of other theoretical work performed both within the framework of the jellium model and beyond, using quantum chemistry methods, and elucidate the level of accuracy of different theoretical approaches. Also, we demonstrate the important role of many-electron correlations in the formation of the structure and properties of small metal clusters. Our results form a good basis for the detailed study of dynamic properties of small metal clusters as well as the structure and properties of other atomic cluster systems.

Our calculations elucidate the level of accuracy of various theoretical schemes for the treatment of electronic structure in metal clusters, which it is important to know and is not obvious in advance because of the complexity of the theoretical methods involved. Some characteristics (dipole and quadrupole moments or spectra of normal vibration modes, for example), which we have calculated in this paper have not been studied before, at least according to our knowledge. These characteristics, however, might be, important, for instance, when considering the dynamics of a cluster beam in an external nonhomogeneous electric or magnetic field. Indeed, cluster multipole moments should be responsible for cluster isomer separation in nonhomogeneous external fields. We analyze the connection between the principal values of the cluster quadrupole moment tensor and the cluster shape (oblate, prolate, or triaxially deformed).

The frequencies of the surface and volume vibration modes have been determined in the spectra of the cluster normal vibration frequencies and their correspondence with the predictions of the dynamical jellium model [41,42] established.

Our calculations have been performed with the use of the GAUSSIAN 98 software package [56]. We have used the atomic system of units in this paper, $\hbar = m_e = |e| = 1$, unless other units are indicated.

II. THEORETICAL METHODS

In this work we study the structure and properties of small sodium clusters on the basis of all-electron *ab initio* many-body theory methods. We calculate the optimized geometries of clusters consisting of up to $N \leqslant 20$ atoms, where N is the number of atoms in the cluster. For the sequence of clusters

with $N \leqslant 20$, we determine the size dependence of the cluster ionization potentials, total energies, multipole moments (dipole and quadrupole), bonding distances, and dipole polarizabilities. We also calculate and analyze the vibration spectra of clusters.

We have done these calculations using different theoretical schemes. We calculated cluster characteristics in the all-electron Hartree-Fock approximation. This approximation does not take into account many-electron correlations in the system, which turn out to play an essential role in the formation of cluster properties. Therefore, we also calculate all the characteristics using post-Hartree-Fock theories accounting for many-electron correlations. This was done in the Møller and Plesset perturbation theory of the second and the fourth order and using the three-parameter Becke gradient-corrected exchange functional with the gradient-corrected correlation functional of Lee, Yang, and Parr (B3LYP).

Note that the post-Hartree-Fock perturbation theories and the density functional approximation are two different theoretical schemes for the solution of many-electron correlation problems based on different physical principles. The important feature of the density functional method consists in the fact that this method takes into account many-electron correlations via a phenomenological exchange-correlation potential. However, so far, there has not been found a unique potential that is universally applicable for different systems and conditions. As a result there is a ''zoo of potentials'' (see, e.g., [68]) valid for special cases. These potentials, of course, do exist in principle as unique quantities but are not actually understood, so alone they cannot serve as a satisfactory basis for achieving a physical interpretation.

Alternatively, one can develop direct *ab initio* methods for the description of electronic properties of metal clusters. This can be achieved by using the Hartree-Fock (HF) approximation and construction on this basis systematic many-body theories such as the random phase approximation with exchange or many-body perturbation theory, an example of which we use in the present work, or the Dyson equation method (see, e.g., [43]). Based on fundamental physical principles, these models can be refined by extending the quality of the approximations, while the physical meaning of the effects included is clearly demonstrated, and thus they often give more accurate and reliable characteristics of metal clusters than does density functional theory. Thus, in the present work, we use both theoretical schemes for calculations and take advantage of the clear physical meaning and reliability of the post-Hartree-Fock perturbation theories and the numerical efficiency of the density functional methods.

Below, we discuss theoretical methods used in our work. The aim of this discussion is to present the essential ideas of the methods and give the necessary references, rather than to describe them in detail.

A. Hartree-Fock method

In the Hartree-Fock approximation, the many-electron wave function of a cluster is expressed as the antisymmetrized product of the single-electron wave functions ψ_i of cluster electrons, which are also often called molecular orbitals. The Hartree-Fock equation for the determination of the molecular orbitals ψ_i reads (see, e.g., [57])

$$(-\Delta/2 + U_{ions} + U_{\mathrm{HF}})\psi_i = \varepsilon_i \psi_i . \tag{1}$$

Here, the first term represents the kinetic energy of the ith electron, and U_{ions} describes its attraction to the ions in the cluster. The Hartree-Fock potential U_{HF} represents the Coulomb and exchange interactions of the electron i with other electrons in the cluster, and ε_i is the single-electron energy.

In GAUSSIAN 98, the molecular orbitals ψ_i are approximated by a linear combination of a predefined set of single-electron functions χ_μ known as basis functions. This expansion reads as follows:

$$\psi_i = \sum_{\mu=1}^{N} c_{\mu i}\chi_\mu , \tag{2}$$

where the coefficients $c_{\mu i}$ are the molecular orbital expansion coefficients, and N is the number of basis functions that are chosen to be normalized.

The basis functions χ_μ are defined as linear combinations of primitive Gaussians:

$$\chi_\mu = \sum_{p} d_{\mu p} g_p , \tag{3}$$

where $d_{\mu p}$ are fixed constants within a given basis set. The primitive Gaussians $g_p = g(\alpha, \mathbf{r})$ are Gaussian-type atomic functions having the following form:

$$g(\alpha, \mathbf{r}) = c x^n y^m z^l e^{-\alpha r^2}. \tag{4}$$

Here, c is the normalization constant. The choice of the integers n, m, and l defines the type of primitive Gaussian function: *s*, *p*, *d*, or *f* (for details, see [58]).

Substituting these expansions in the Hartree-Fock equations (1), one can rewrite them in the form (known also as the Roothaan and Hall equations)

$$\sum_{\nu=1}^{N} (H_{\mu\nu} - \varepsilon_i S_{\mu\nu}) c_{\nu i} = 0, \quad \mu = 1,2,\ldots,N. \tag{5}$$

Written in the matrix form, this equation reads

$$HC = SC\varepsilon, \tag{6}$$

where each element is a matrix. Here, ε is a diagonal matrix of orbital energies, each of its elements ε_i is the single-electron energy of the molecular orbital ψ_i, H is the Hamiltonian matrix as follows from Eq. (1), and S is the overlap matrix, describing the overlap between orbitals. For more details regarding this formalism, see [58]. Equations (6) are nonlinear and must be solved iteratively. The procedure which does so is called the *self-consistent field* method.

The equations written above refer to the restricted Hartree-Fock method. For open shell systems, the unrestricted Hartree-Fock method has to be used. In this case, the

α and β electrons with spins up and down are assigned to different orbitals, resulting in two sets of molecular orbital expansion coefficients:

$$\psi_i^\alpha = \sum_{\mu=1}^{N} c_{\mu i}^\alpha \chi_\mu ,$$

$$\psi_i^\beta = \sum_{\mu=1}^{N} c_{\mu i}^\beta \chi_\mu . \tag{7}$$

The two sets of coefficients result in two sets of Hamiltonian matrices and two sets of orbitals.

B. Møller-Plesset perturbation theory method

The Hartree-Fock theory provides an inadequate treatment of electron motion within a molecular system, because it does not properly treat many-electron correlations. The many-electron correlations can be accounted for using different methods. The most straightforward way to achieve this goal is based on perturbation theory. Indeed, the total Hamiltonian H of the cluster can be divided into two parts:

$$H = H_0 + V. \tag{8}$$

Here H_0 is the Hamiltonian corresponding to the Hartree-Fock level of theory and V is the residual interelectron interaction, which can be treated as a small perturbation.

Considering V as a small perturbation one can construct the solution of the Schrödinger equation for a many-electron system in an arbitrary order of perturbation theory. Perturbation theory of this type is well known since the work by Møller and Plesset [59] and can be found in numerous textbooks on quantum mechanics (see, e.g., [60]).

Below we refer to this theoretical method as to the Møller-Plesset (MP) perturbation theory [59] of the second or fourth order, MP_2 or MP_4. Indices here indicate the order of the perturbation theory.

C. Density functional methods

The density functional theory (DFT) is based upon a strategy of modeling electron correlation via general functionals of the electron density. Within the DFT one has to solve the Kohn-Sham equations, which read (see, e.g., [8,9,11–14])

$$\left(\frac{\hat{p}^2}{2} + U_{ions} + V_H + V_{xc} \right) \psi_i = \varepsilon_i \psi_i , \tag{9}$$

where the first term represents the kinetic energy of the ith electron, U_{ions} describes its attraction to the ions in the cluster, V_H is the Hartree part of the interelectronic interaction,

$$V_H(\mathbf{r}) = \int \frac{\rho(\mathbf{r}')}{|\mathbf{r}-\mathbf{r}'|} d\mathbf{r}', \tag{10}$$

and $\rho(\mathbf{r}')$ is the electron density,

$$\rho(\mathbf{r}) = \sum_{\nu=1}^{N} |\psi_i(\mathbf{r})|^2, \tag{11}$$

where V_{xc} is the local exchange-correlation potential, ψ_i are the electronic orbitals, and N is the number of electrons in the cluster.

The exchange-correlation potential is defined as the functional derivative of the exchange-correlation energy functional

$$V_{xc} = \frac{\delta E_{xc}[\rho]}{\delta \rho(\mathbf{r})}. \tag{12}$$

The approximate functionals employed by DFT methods partition the exchange-correlation energy into two parts, referred to as the *exchange* and *correlation* parts

$$E_{xc}[\rho] = E_x(\rho) + E_c(\rho). \tag{13}$$

Physically, these two terms correspond to same-spin and mixed-spin interactions, respectively. Both parts are functionals of the electron density, which can be of two distinct types: either a *local* functional depending on only the electron density ρ or a *gradient-corrected* functional depending on both ρ and its gradient $\nabla\rho$.

In the literature, there is a variety of exchange-correlation functionals. Below, we refer only to those that are related to the calculation performed in this work.

The local exchange functional is virtually always defined as follows:

$$E_x^{LDA} = -\frac{3}{2}\left(\frac{3}{4\pi}\right)^{1/3} \int \rho^{4/3} d^3\mathbf{r}. \tag{14}$$

This form was developed to reproduce the exchange energy of a uniform electron gas. By itself, however, it is not sufficient for the adequate description of atomic clusters.

The gradient-corrected exchange functional introduced by Becke [61] and based on the LDA exchange functional reads

$$E_x^{B88} = E_x^{LDA} - \gamma \int \frac{\rho^{4/3} x^2}{1 + 6\gamma \sinh^{-1} x} d^3\mathbf{r} \tag{15}$$

where $x = \rho^{-4/3}|\nabla\rho|$ and $\gamma = 0.0042$ is a parameter chosen to fit the known exchange energies of the noble gas atoms.

Analogous to these exchange functionals, there are local and gradient-corrected correlation functionals, for example, those introduced by Perdew and Wang (see, e.g., [62] and references therein) and by Lee, Yang, and Parr [63]. Their explicit expressions are somewhat lengthy and thus we do not present them here, referring readers to the original papers.

In pure DFT, an exchange functional usually pairs with a correlation functional. For example, the well-known BLYP functional pairs Becke's gradient-corrected exchange functional (15) with the gradient-corrected correlation functional of Lee, Yang, and Parr [63].

In spite of the success of the pure DFT theory in many cases, one has to admit that the Hartree-Fock theory accounts

for the electron exchange more naturally and precisely. Thus, Becke has suggested [61] functionals which include a mixture of Hartree-Fock and DFT exchange along with DFT correlations, conceptually defining E_{xc} as

$$E_{xc}^{mix}=c_{\mathrm{HF}}E_x^{\mathrm{HF}}+c_{DFT}E_{xc}^{DFT}, \tag{16}$$

where c_{HF} and c_{DFT} are constants. Following this idea, a Becke-type three-parameter functional can be defined as follows:

$$E_{xc}^{B3LYP}=E_x^{LDA}+c_0(E_x^{\mathrm{HF}}-E_X^{LDA})+c_x(E_x^{B88}-E_x^{LDA}) +E_c^{VWN3}+c_c(E_c^{LYP}-E_c^{VWN3}). \tag{17}$$

Here, $c_0=0.2$, $c_x=0.72$, and $c_c=0.81$ are constants, which were defined by fitting to the atomization energies, ionization potentials, proton affinities, and first-row atomic energies [58]. E_x^{LDA} and E_x^{B88} are defined in Eqs. (14) and (15), respectively. E_x^{HF} is the functional corresponding to the Hartree-Fock equations (1). The explicit form for the Vosko-Wilk-Nusair correlation functional E_c^{VWN3} as well as for the gradient-corrected correlation functional of Lee, Yang, and Parr, E_c^{LYP}, can be found in [64] and [63], respectively. Note that instead of E_c^{VWN3} and E_c^{LYP} in Eq. (17) one can also use the Perdew and Wang correlation functional (see, e.g., [62] and references therein).

D. Geometry optimization

The cluster geometries that we have calculated in our work have been determined using a geometry optimization procedure. This procedure implies calculation of the multidimensional potential energy surface for a cluster and then finding local minima on this surface. The key point for this search is fixing the starting geometry of the cluster, which might converge during the calculation to the local or global minimum. There is no unique way to achieve this goal with GAUSSIAN 98.

In our calculations, we have created the starting geometries empirically, often assuming certain cluster symmetries. Note that during the optimization process the geometry of the cluster as well as its initial symmetry sometimes change dramatically. All the characteristics of clusters that we have calculated and present in the next section are obtained for clusters with optimized geometry.

In our calculations, we have made no assumptions about the core electrons in the optimized clusters, which means that all electrons available in the system, have been taken into account when computing the potential energy surface. For clusters with $N>10$, this process becomes rather computer time demanding. Thus, in this work we have limited our calculations to clusters up to $N\leqslant 20$.

E. Normal vibrations

Knowledge of the potential energy surface in the vicinity of a local minimum allows one easily to determine the corresponding normal vibration modes of the system. We have performed this calculation and determined the vibration energy spectrum for a number of clusters. In this calculation particular attention has been paid to the identification of the breathing and surface vibration modes, and their frequencies have been compared with those predicted in [41,42] for spherical sodium clusters on the basis of the dynamical jellium model.

III. RESULTS OF CALCULATIONS AND DISCUSSION

In this section we present the results of calculations performed with the use of the methods described above. We calculated the optimized geometries of neutral and singly charged sodium clusters consisting of up to 20 atoms, their multipole moments (dipole and quadrupole), static polarizabilities, binding energies per atom, ionization potentials, and frequencies of the normal vibration modes. We compare the results of our calculations with the available experimental data and the results of other theoretical works performed both within the framework of the jellium model and beyond, using quantum chemistry methods, and establish the level of accuracy of different theoretical approaches. Particular attention is paid to clusters in the range $10<N<20$, because some characteristics of the clusters in this size range have been calculated on an *ab initio* basis in our paper for the first time to our knowledge. Also, we demonstrate the important role of many-electron correlations in the formation of the structure and properties of small metal clusters.

A. Geometry optimization of Na_n and Na_n^+ clusters

Results of the cluster geometry optimization for neutral and singly charged sodium clusters consisting of up to 20 atoms are shown in Figs. 1 and 2, respectively. The cluster geometries were determined using the methodology described in Sec. II; namely, the optimization of the cluster geometries was performed with the use of B3LYP and MP_2 methods.

For clusters with $N\leqslant 6$, we preferably used the MP_2 method. This method leads to results that are in reasonable agreement with those derived by other methods (see, e.g., [16,17]). For example, the side bond length in the rhomboidal Na_4 cluster calculated in [16] by the all-electron Hartree-Fock method is equal to 3.74 Å, while in our case it is equal to 3.56 Å. The smaller diagonal value for Na_4 is equal to 3.25 Å in [16], while we determine it as 3.18 Å.

The MP_2 method becomes more and more computer time demanding with growth in cluster size. This happens due to increase in the number of integrals involved in the computations. It turns out that for larger cluster systems the B3LYP method is more efficient. The accuracy of the B3LYP method is comparable to the accuracy of the MP_2 method, as is clear from the comparison of the B3LYP and MP_2 cluster geometries with those computed in [16] by the configuration interaction method.

Clusters of a certain size can possess various isomeric forms, whose number grows dramatically with increasing cluster size. We illustrate the situation and calculate several isomers of the Na_3, Na_6, Na_{10}, Na_{11}, and Na_{20} clusters. They are all presented in Fig. 1. Note that the linear and equilateral triangular Na_3 isomers were not described in the

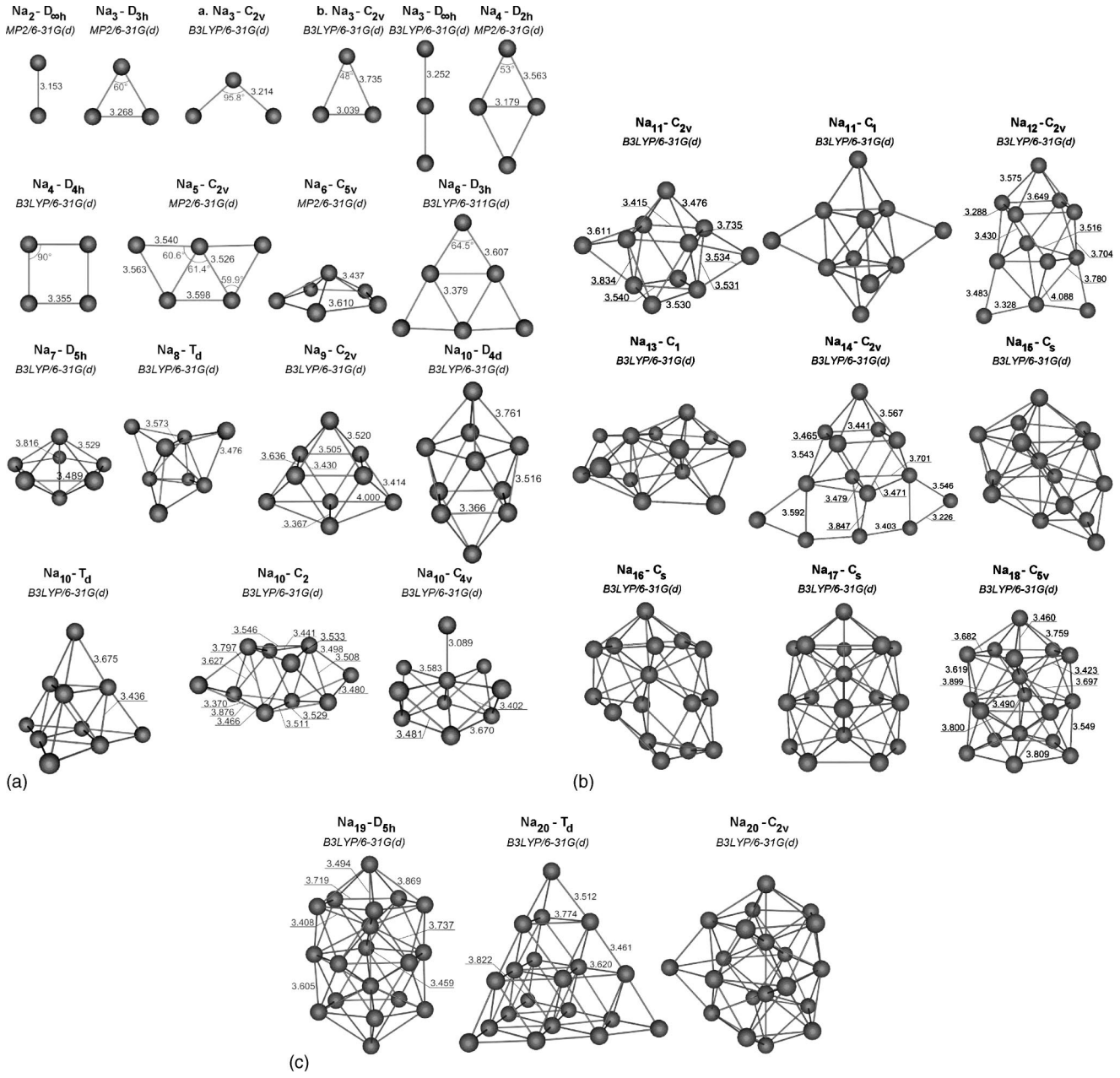

FIG. 1. Optimized geometries of neutral sodium clusters Na_2–Na_{10} (a), Na_{11}–Na_{18} (b), and Na_{19} and Na_{20} (c). The interatomic distances are given in angstroms. The label above each cluster image indicates its point symmetry group and the calculation method by which the cluster was optimized.

earlier papers [15–17] (see also [11,13,14]), in which isosceles triangular isomers were considered. A comparison of the properties (dipole and quadrupole moments, total energies, bonding distances) of these clusters will be given below.

Using the example of the Na_4 cluster, we demonstrate how the multiplicity of an electronic state of the system can influence its geometry. Figure 1 shows that the Na_4 cluster has the rhomboidal geometry corresponding to the D_{2h} point symmetry group, if the multiplicity of the cluster is equal to 1, while, if the multiplicity is equal to 3, the cluster has the quadratic geometry characterized by the D_{4h} point symmetry group.

Sodium clusters with $N \leqslant 5$ have a plane structure, while for $N=6$ both plane and spatial isomers are possible. This feature is consistent with the jellium picture and can be explained by the minimization principle for the cluster surface. Indeed, the surface of small plane cluster isomers is smaller than the surface of possible three-dimensional forms.

A comparison of the geometries of the neutral and singly charged clusters presented in Figs. 1 and 2 shows significant differences. For smaller sizes ($N \leqslant 8$), singly charged and neutral clusters sometimes have different point symmetry groups and bonding distances (see images of the Na_4, Na_5, Na_6, and Na_8 clusters and their ions). The alteration in the geometry of cluster ions occurs due to the excess positive

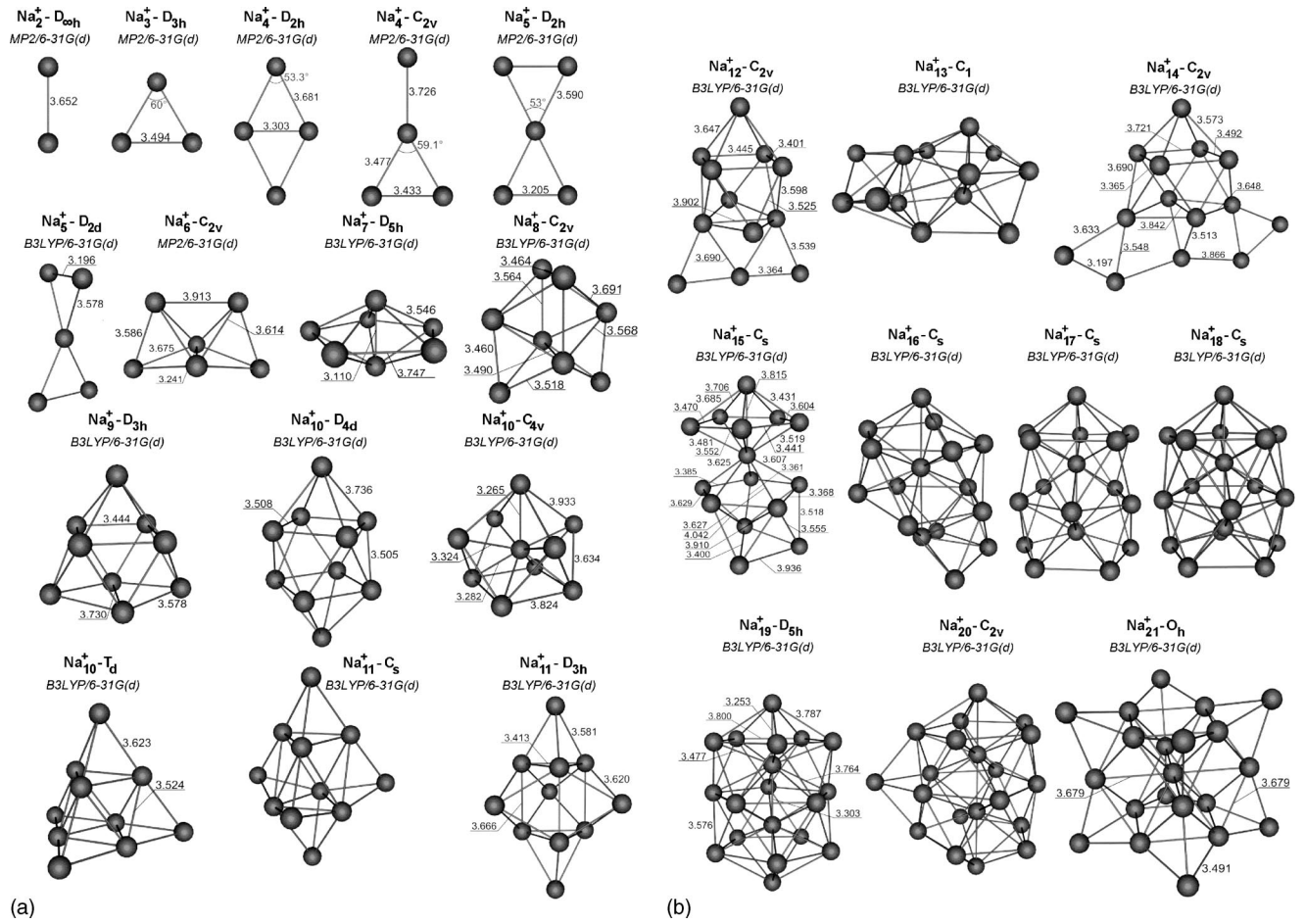

FIG. 2. Optimized geometries of singly charged sodium clusters Na_2^+–Na_{11}^+ (a) and Na_{12}^+–Na_{21}^+ (b). The interatomic distances are given in angstroms. The label above each cluster image indicates the point symmetry group and the calculation method by which the cluster was optimized.

charge available in the system. The structural changes of cluster ions become less profound with increasing cluster size (see clusters with $N \geqslant 10$), because the excess positive charge in this case turns out to be insufficient to produce substantial change in a massive cluster, although sometimes (compare Na_{15} and Na_{15}^+) noticeable change in the cluster geometry is also possible.

The striking difference in the geometries of small singly charged and neutral clusters is closely linked to the problem of cluster fission. It is natural to assume that with increasing cluster charge small clusters should become unstable and fragment into two parts, while for larger cluster sizes one can expect quasistable configurations, which should decay via the fission process. Calculation of such configurations is an interesting task, because it may provide essential information on the predominant fission channels in the system. We do not perform such an analysis in our work, but point out that the geometries of cluster ions like Na_4^+, Na_5^+, Na_6^+, and Na_{15}^+ give obvious hints on the possible fragmentation channels in these cluster systems.

Figure 1 shows that the clusters Na_8 and Na_{20} have higher point symmetry group T_d than to the other clusters. This result is in qualitative agreement with the jellium model. According to the jellium model [36–40], clusters with closed shells of delocalized electrons have a spherical shape, while clusters with open electron shells are deformed. The jellium model predicts spherical shapes for the clusters with the magic numbers $N=8,20,34,40,\ldots$, having respectively the following electronic shells filled: $1s^2 1p^6, 1d^{10} 2s^2, 1f^{14}, 2p^6, \ldots$.

We have also found the T_d symmetry group isomer for the Na_{10} cluster. However, this cluster isomer is not the lowest energy isomer of Na_{10} (see Table I in the Appendix). A similar situation occurs in the jellium model, where the $1s^2 1p^6, 2s^2$ closed shell electronic configuration does not minimize the cluster total energy.

Note also that both the local density approximation and HF jellium models predict some deviation from sphericity for the Na_{18} cluster [40], which has the $1d$ subshell filled, as a result of electron configuration mixing. This fact is also in qualitative agreement with the results of our *ab initio* calculations. The point group symmetry of the Na_{18} cluster, C_{5v}, is lower than T_d, which is the point symmetry group for the Na_8 and Na_{20} clusters, and even lower than the point symmetry group for some open shell clusters, like Na_7 and Na_{19}, which have the point symmetry group D_{5h}.

Note that there are some clusters possessing relatively low point symmetry group that nevertheless are quite close to a

higher point symmetry group. The higher symmetry breaking can be explained via the Jahn-Teller effect [60]. This situation occurs, for example, in the Na_9 and Na_{11} clusters, which possess the C_{2v} point symmetry group, but their geometry is close to the geometry of the D_{3h} group.

The jellium prediction on the sphericity of the magic clusters does not work so well for cluster ions. Indeed, the geometry and the point symmetry group of Na_9^+ do not allow one to infer the higher sphericity of this cluster as compared to its neighbors. The analysis of the quadrupole moments and cluster deformations performed below demonstrates this conclusion quite clearly. This happens because the forces emerging in the cluster during its transition from neutral to singly charged state turn out to be insufficient to rearrange the cluster geometry from a deformed to a spherical one.

We have found two isomers of the Na_{20} cluster that have rather regular structure and differ significantly one from another. The cluster geometries presented in Fig. 1 allow one to assume that there exist at least two independent paths to cluster structure formation. Indeed, the isomers

$$\mathrm{Na}_6^{C_{5v}} \rightarrow \mathrm{Na}_7 \rightarrow \mathrm{Na}_{10}^{C_{4v}} \rightarrow \mathrm{Na}_{13} \rightarrow \mathrm{Na}_{15} \rightarrow \mathrm{Na}_{16} \rightarrow \mathrm{Na}_{17} \rightarrow \mathrm{Na}_{18} \rightarrow \mathrm{Na}_{19} \rightarrow \mathrm{Na}_{20}^{C_{2v}}$$

probably belong to the chain leading to the formation of the C_{2v} isomer of the Na_{20} cluster, while the clusters

$$\mathrm{Na}_6^{D_{3h}} \rightarrow \mathrm{Na}_8 \rightarrow \mathrm{Na}_9 \rightarrow \mathrm{Na}_{10}^{T_d} \rightarrow \mathrm{Na}_{11}^{C_1} \rightarrow \mathrm{Na}_{12} \rightarrow \mathrm{Na}_{14} \rightarrow \mathrm{Na}_{20}^{T_d}$$

form the path by which the T_d isomer of the Na_{20} cluster is formed. Figure 1 clearly shows the steps of the cluster formation process along these two paths. Although for most N we have calculated isomers belonging to one path or another, it is natural to assume that the two different types of geometry exist for all N, as for Na_6 and Na_{20} clusters. For clusters smaller than Na_6, one cannot distinguish the two paths clearly enough as is seen from Fig. 1. Conclusions made for neutral clusters regarding the growth process are applicable to a great extent to singly charged cluster ions as is clear from Fig. 2, although cluster ion geometries sometimes differ substantially from their neutral prototypes.

Cluster geometries allow one easily to compute and analyze the average bonding distance as a function of cluster size. The result of this analysis for neutral and singly charged sodium clusters is presented in Figs. 3 and 4. These figures show how the average bonding distance converges to the bulk limit indicated in the figures by horizontal lines. When calculating the average bonding distance in a cluster, only interatomic distances smaller than 4.1 Å have been considered. This upper limit on the interatomic distances was chosen as a distance that is 10% larger than the bcc lattice nearest neighbor distance in bulk sodium.

Figures 3 and 4 show that the dependence of the average bonding distance $\langle R \rangle$ on cluster size is nonmonotonic. For neutral clusters, one can see odd-even oscillations of $\langle R \rangle$ atop its systematic growth and approach to the bulk limit.

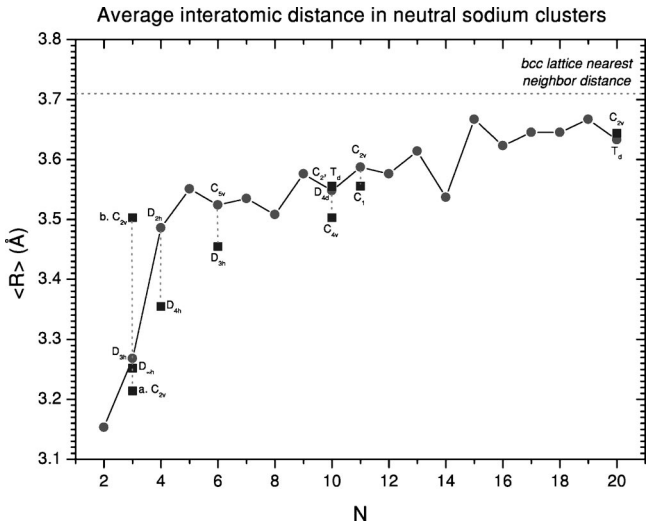

FIG. 3. Averaged bonding distance as a function of cluster size for optimized geometries of neutral sodium clusters. For some cluster numbers more than one isomer has been considered. In these cases, labels indicate the point symmetry group of the corresponding isomers. Geometries of the optimized clusters can be found in Fig. 1.

These features have a quantum origin and can be explained by the delocalization of the valence atomic electrons. Indeed, the odd-even oscillations arise due to the spin pairing of the delocalized electrons. This type of behavior is also typical of other cluster characteristics and will be discussed below in more detail. The reason for the relatively large increase of the average distance seen for small sodium cluster ions with $N \leqslant 9$ is also qualitatively clear. It can be explained by the Coulomb instability developing in the cluster with increasing ionization rate.

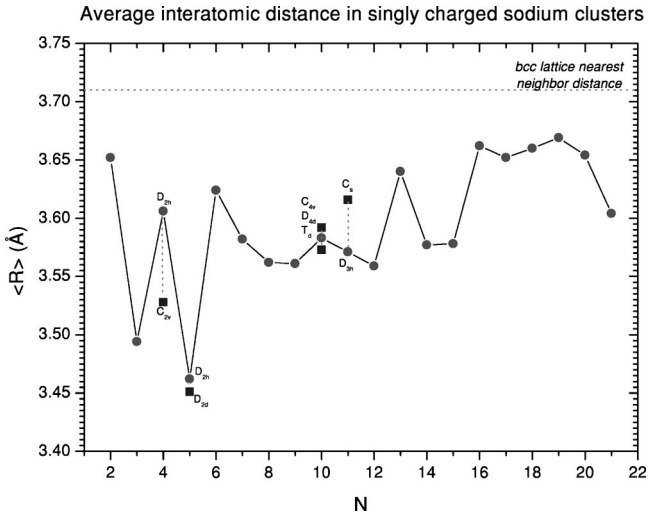

FIG. 4. Averaged bonding distance as a function of cluster size for optimized geometries of singly charged sodium clusters. For some cluster numbers more than one isomer has been considered. In these cases, labels indicate the point symmetry group of the corresponding isomers. Geometries of the optimized clusters can be found in Fig. 2.

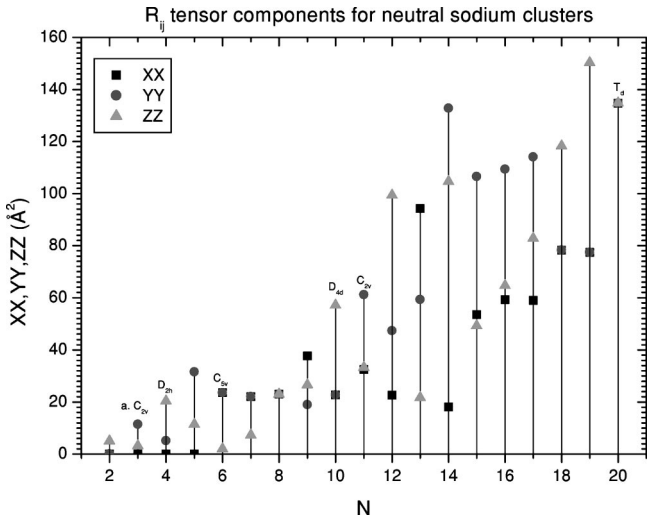

FIG. 5. The principal values of the tensor R_{ij} for optimized neutral sodium clusters as a function of cluster size calculated by the B3LYP method. Squares, circles, and triangles represent the R_{xx}, R_{yy}, and R_{zz} tensor principal values, respectively. For some clusters, more than one isomer has been considered. In these cases, labels indicate the point symmetry group of the corresponding isomers. Geometries of the optimized clusters can be found in Fig. 1.

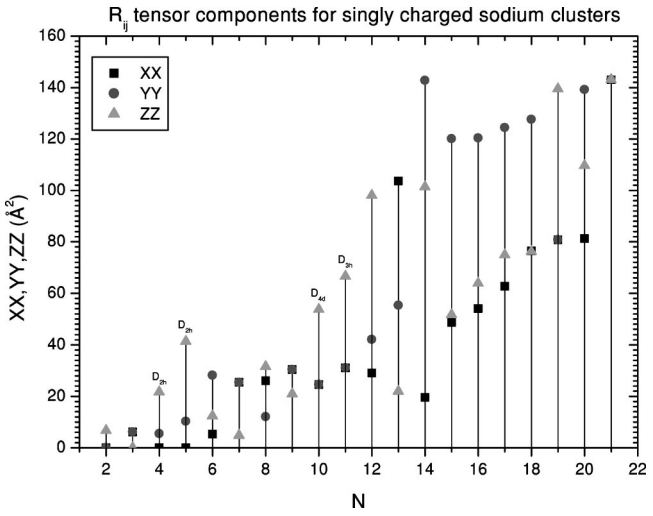

FIG. 6. Principal values of the tensor R_{ij} for optimized singly charged sodium clusters as a function of cluster size calculated by the B3LYP method. Squares, circles, and triangles represent the R_{xx}, R_{yy}, and R_{zz} tensor principal values, respectively. For some clusters, more than one isomer has been considered. In these cases, labels indicate the point symmetry group of the corresponding isomers. Geometries of the optimized clusters can be found in Fig. 2.

The cluster shape can be characterized by the oblate, prolate, or triaxial deformation. The prolate deformation of the cluster is characterized by a larger distortion of the ionic charge distribution along the z axis as compared to distortions along the x and y axes. In the oblate deformation case the situation is opposite. Deformations of the ionic charge distribution in the x and y directions are larger than in the z direction. In both cases the deformations along x and y directions are equal. The triaxial shape deformation is characterized by unequal distortions of the ionic charge distribution along x, y, and z directions. Often, however, two of the three deformations are close to each other and this allows one to discuss the triaxially deformed prolate or oblate cases. Knowledge of the type of cluster deformation is quite useful for comparison with the jellium model results and analysis of metal cluster photon absorption spectra (see [13]).

The type of cluster deformation can be easily determined by the principal values of the tensor $R_{ij}=\Sigma x_i x_j$. Here, the summation is performed over all ions in the system. The principal values of this tensor R_{xx}, R_{yy}, and R_{zz} define the dimensions R_x, R_y, and R_z of the ionic charge distribution in the cluster along the principal axes x, y, and z via the relations $R_x=\sqrt{R_{xx}/N}$, $R_y=\sqrt{R_{yy}/N}$, and $R_z=\sqrt{R_{zz}/N}$. Note that the tensor R_{ij} is closely connected to the cluster moment of inertia tensor and the quadrupole moment tensor of the ionic distribution.

In Figs. 5 and 6 we present the principal values R_{xx}, R_{yy}, and R_{zz} for a sequence of neutral and singly charged clusters, respectively. Figures 5 and 6 demonstrate how the cluster deformation changes as a function of cluster size. Figure 5 shows that all three principal values are equal for the tetrahedral group isomers of the magic clusters Na_8 and Na_{20}. This feature is in qualitative agreement with the jellium model, which predicts spherical shapes for the magic clusters. In many cases two of the three principal values of R_{ij} are equal or nearly equal. Using the definition of the prolate and oblate cluster distortions given above and Figs. 5 and 6, one can easily determine the type of cluster deformation. For example, the clusters Na_2, Na_{10}, Na_{18}, and Na_{19} have the prolate deformation along the z principal axis, because the condition $R_{xx}=R_{yy}<R_{zz}$ is satisfied. The clusters Na_6 and Na_7 possess the prolate deformation because in this case $R_{xx}=R_{yy}>R_{zz}$. Figures 5 and 6 show that most of the clusters are triaxially deformed. However, it is often possible to assign clusters the triaxially deformed prolate or oblate shape, because two of the three principal values are close to each other. Thus, for instance, Na_4 are Na_{15} are triaxially prolate clusters, while Na_{14} is a triaxially oblate one. Figures 5 and 6 also show the relative values of prolate and oblate deformations in various clusters.

One can define a tensor analogous to R_{ij}, but for electrons. We do not plot the principal values of this tensor because they are very close in absolute value to the principle values shown in Figs. 5 and 6 and can be traced from the principal values of the cluster total quadrupole moment tensor considered below in Sec. III D.

B. Binding energy per atom for small neutral and singly charged sodium clusters

The binding energy per atom for small neutral and singly charged sodium clusters is defined as follows:

$$E_b/N=E_1-E_N/N, \tag{18}$$

$$E_b^+/N=((N-1)E_1+E_1^+-E_N^+)/N, \tag{19}$$

where E_N and E_N^+ are the energies of a neutral and singly

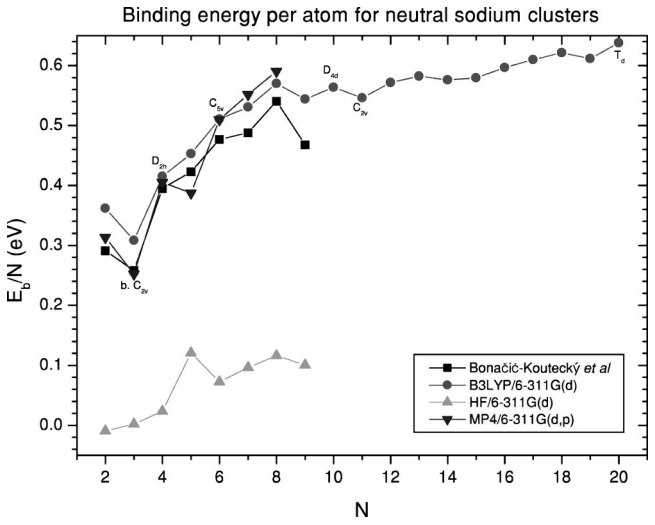

FIG. 7. Binding energy per atom for neutral sodium clusters as a function of cluster size. Circles represent the binding energies per atom calculated by the B3LYP method; lower and upper triangles correspond to the energies obtained by the MP_4 method and in the HF approximation respectively. Squares show the results of the configuration-interaction approach from the work by Bonačić-Kotecký *et al.* (for details see [16,18]). Some points in the figure have labels indicating the point symmetry group of the isomers represented. Geometries of the corresponding clusters can be found in Fig. 1.

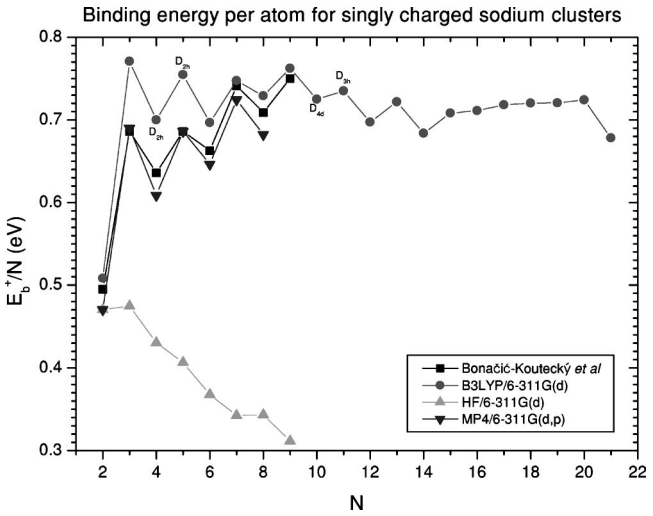

FIG. 8. Binding energy per atom for singly charged sodium clusters as a function of cluster size. Circles represent the binding energies per atom calculated by the B3LYP method; lower and upper triangles correspond to the energies obtained by the MP_4 method and in the HF approximation, respectively. Squares show the results of the configuration-interaction approach from the work by Bonačić-Kotecký *et al.* (for details see [16,18]). Some points in the figure have labels indicating the point symmetry group of the isomers represented. Geometries of the corresponding clusters can be found in Fig. 2.

charged N-particle atomic cluster, respectively. E_1 and E_1^+ are the energies of a single sodium atom and an ion.

Figures 7 and 8 show the dependence of the binding energy per atom for neutral and singly charged clusters as a function of cluster size. The energies of the clusters have been computed using the B3LYP, MP_4, and HF methods described in Sec. II. For clusters with $N \leqslant 8$, computations of the energies have been performed by the three methods for the sake of comparison. We wanted to compare the methods for their accuracy and computation efficiency. The results of our calculations have also been compared with those derived by the configuration interaction (CI) method in [15–17]. Figures 7 and 8 demonstrate that the results of the MP_4 and B3LYP methods are in reasonable agreement with each other and with the CI results. The HF points significantly differ from the MP_4, B3LYP, and CI ones, which demonstrates the importance of many-electron correlations, taken into account in the MP_4, B3LYP and CI methods and omitted in the HF approximation. Note that the energy of Na_2, if computed in the pure HF approximation, is close to zero, which means that bonding in this molecule takes place mainly due to many-electron correlations.

The energies of clusters larger than Na_8 and Na_8^+ have been computed by the B3LYP method only, because this method is more efficient than MP_4 and the accuracy of both methods is comparable.

Figures 7 and 8 demonstrate the even-odd oscillation behavior in the dependence of binding energy on cluster size. Indeed, for singly charged clusters, odd numbers corresponding to the singlet multiplicity have higher energies as compared to their even neighbors. An analogous situation takes place for neutral clusters. In this case, even cluster numbers have higher binding energies as compared to their odd neighbors. Note that for neutral clusters this phenomenon occurs simultaneously with a slight systematic growth of the binding energies per atom with increasing cluster size.

Figures 7 and 8 also show that the binding energy per atom in the magic neutral clusters Na_8 and Na_{20} is a little higher as compared to other clusters of similar size. A similar situation occurs for the Na_9^+ cluster in the ionic case. This feature can be qualitatively understood on the basis of the jellium model: the increase in the magic cluster binding energy takes place due to the delocalized electron shell closure. Note that the binding energy per atom for the magic Na_{21}^+ turns out to be smaller than that for the neighboring cluster ions. This happens because this particular cluster ion isomer is characterized by the O_h point symmetry group. Cluster isomers based on this point symmetry group usually have lower binding energy per atom as compared to isomers based on icosahedral point symmetry group like those with $N \geqslant 13$ shown in Figs. 1 and 2.

Tables I and II given in the Appendix provide accurate values of the cluster total energies calculated by MP_4, B3LYP, and HF methods. For neutral clusters with $N \leqslant 8$, we also present the cluster energies calculated in [16] by the CI method. The values given in these tables have been used to plot Figs. 7 and 8. For some clusters, the energies of different symmetry isomers are also given in the tables.

C. Ionization potentials

Let us now consider how the ionization potentials of sodium clusters evolve with increasing cluster size. Experi-

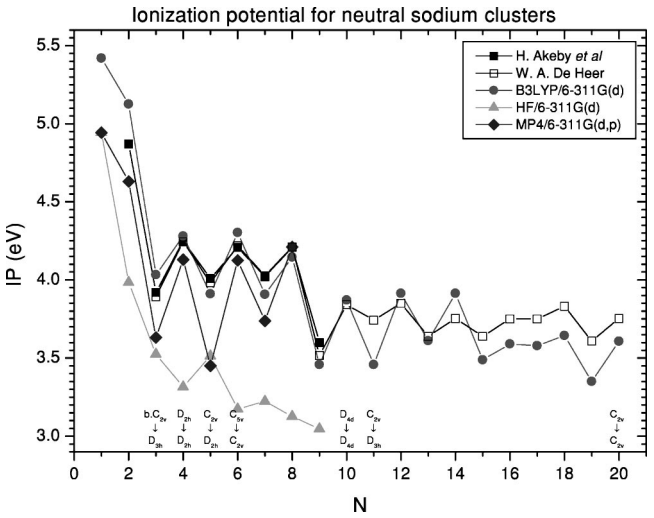

FIG. 9. Ionization potentials of neutral sodium clusters as a function of cluster size. Circles show the results derived by the B3LYP method. Triangles and rhomboids represent the ionization potentials calculated by the HF and MP_4 methods, respectively. Filled and open squares are the experimental values taken from [20] and [8], respectively. For some clusters, more than one neutral and/or singly charged cluster isomer has been considered. In these cases, labels indicate the point symmetry group of the initial neutal and the final charged cluster isomers used for the calculation of the ionization potential.

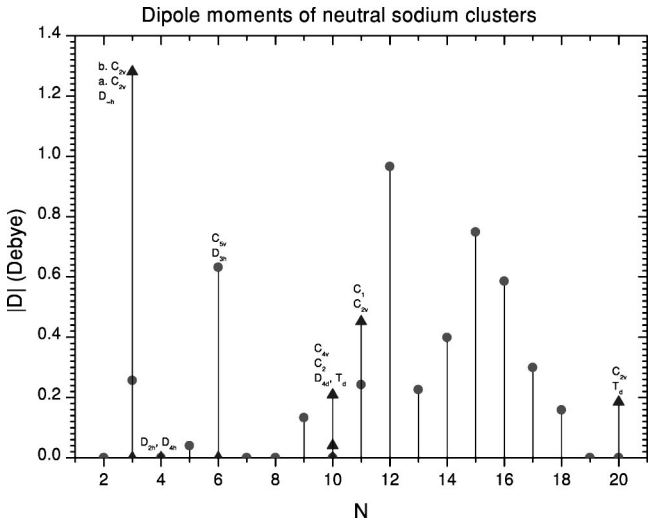

FIG. 10. Dipole moments of the optimized neutral sodium clusters as a function of cluster size calculated by the B3LYP method. For some clusters, more than one isomer has been considered. In these cases, labels indicate the point symmetry group of corresponding isomers. Geometries of the optimized clusters can be found in Fig. 1. 1 D=0.3935 a.u.

mentally, this dependence was measured for sodium clusters in [8,20].

The ionization potential V_i of a cluster consisting of N atoms is defined as the difference between the energies of the singly charged and neutral clusters:

$$V_i = E_N^+ - E_N . \tag{20}$$

Figure 9 shows the dependence of the cluster ionization potential on N. Figure 9 demonstrates the comparison of the results derived by the different methods B3LYP, MP_4, and HF (see Sec. II) with the experimental data from [8] and [20]. The results of the B3LYP and MP_4 methods are in reasonable agreement with the experimental data, while the ionization potentials calculated on the basis of the HF approximation differ substantially from the experimental observations. This comparison shows the role of many-electron correlations in the formation of the cluster ionization potentials. The correlation effects are taken into account by the B3LYP and MP_4 methods and omitted in the HF approximation.

Figure 9 demonstrates that the ionization potentials drop with increasing cluster size, which is consistent with predictions of the classical spherical droplet model. However, this process has many irregularities, which have a quantum origin. Indeed, the dependences derived by the MP_4 and B3LYP methods as well as the experimental one have a prominent odd-even oscillatory tendency. The maxima in these dependencies correspond to the even-N clusters, which means their higher stability as compared to the neighboring odd-N clusters. This happens because the multiplicities of the even- and odd-N clusters are different, being equal to 1 and 2, respectively. Interestingly enough, the B3LYP method reproduces correctly even the experimentally observed irregularity in the odd-even oscillatory behavior, that happens at $N=16$ and $N=17$, and some other minor details of the experimental data.

A significant steplike decrease in the ionization potential value happens at the transition from the dimer to the trimer cluster and also in the transition from Na_8 to Na_9. Such irregular behavior can be explained by the closure of the electronic $1s$ and $1p$ shells of the delocalized electrons in the clusters Na_2 and Na_8, respectively. The next significant drop in the ionization potential value takes place in the transition from the magic Na_{20} to the Na_{21} cluster.

D. Multipole moments

We have calculated multipole moments (dipole, quadrupole, octapole, and hexadecapole) for the sodium clusters whose geometry is shown in Figs. 1 and 2. In Figs. 10 and 11, we plot the absolute values of the dipole moments for neutral and singly charged sodium clusters as a function of cluster size.

The dipole moments of some sodium clusters (see Fig. 10), that we predict here arise due to the fact that the electron charge distribution does not always match the ionic charge distribution and can be shifted with respect to the cluster center of mass. Our calculations show that only clusters with C point symmetry groups, like the isosceles triangle isomers of Na_3, the pentagonal Na_6 pyramid isomer, Na_{12}, Na_{18}, and others, possess dipole moments. These clusters have either an axis of a certain order or a plane of symmetry, but no perpendicular symmetry elements (planes or axes). This rule remains correct even for the Na_{20} cluster isomer with the symmetry C_{2v}, which has the closed shell configuration

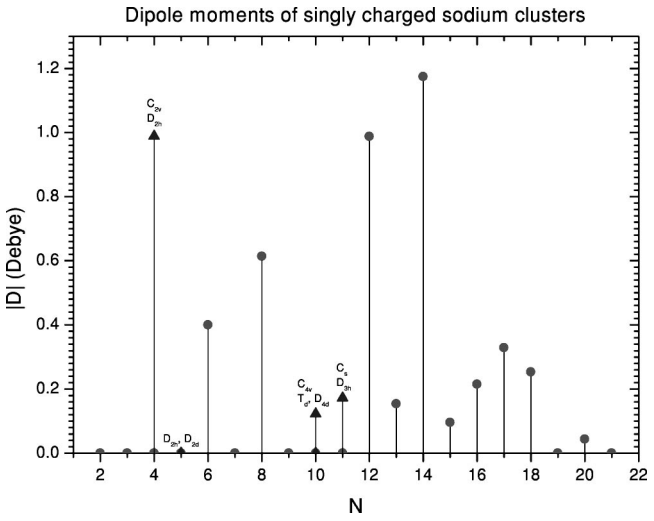

FIG. 11. Dipole moments for the optimized singly charged sodium clusters as a function of cluster size calculated by the B3LYP method. For some clusters, more than one isomer has been considered. In these cases, labels indicate the point symmetry group of corresponding isomers. Geometries of the optimized clusters can be found in Fig. 2.

$1s^2 1p^6 1d^{10} 2s^2$ of delocalized electrons according to the jellium model. The geometries of the cluster ions differ significantly from the geometries of the corresponding neutral clusters, but the rule formulated above for the appearance of the cluster dipole moments remains valid in this case also, as is clear from Fig. 11.

The principal values of the quadrupole moments, tensor for optimized neutral and singly charged clusters are presented in Figs. 12 and 13, respectively. For clusters with an

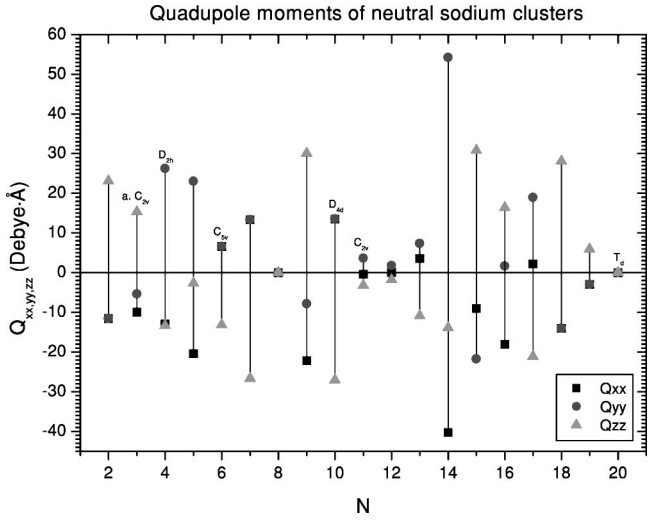

FIG. 12. Principal values of the quadrupole moment tensor for the optimized neutral sodium clusters as a function of cluster size calculated by the B3LYP method. Squares, circles and triangles represent the Q_{xx}, Q_{yy}, and Q_{zz} tensor principal values, respectively. For some clusters, more than one isomer has been considered. In these cases, labels indicate the point symmetry group of corresponding isomers. Geometries of the optimized clusters can be found in Fig. 1.

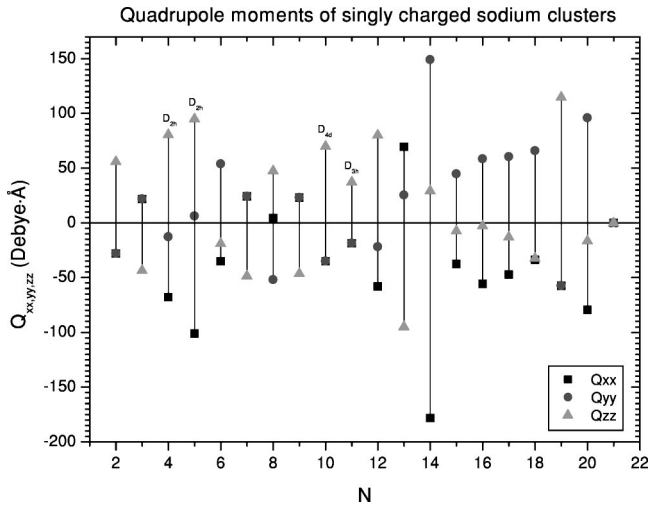

FIG. 13. Principal values of the quadrupole moment tensor for the optimized singly charged sodium clusters as a function of cluster size calculated by the B3LYP method. Squares, circles, and triangles represent the Q_{xx}, Q_{yy}, and Q_{zz} tensor principal values, respectively. For some clusters, more than one isomer has been considered. In these cases, labels indicate the point symmetry group of corresponding isomers. Geometries of the optimized clusters can be found in Fig. 2.

axis of symmetry, this axis has been chosen as the z axis of the coordinate system, in which the calculation of the quadrupole moments was performed. The quadrupole moment tensor is defined as the average value of the following operator:

$$Q_{ij} = \sum q(3x_i x_j - \delta_{ij}\mathbf{r}^2). \tag{21}$$

Here, the summation is performed over all electronic and ionic charges in the cluster. Note that the trace of the tensor Q_{ij} is equal to zero.

The ionic part of Q_{ij} can be expressed via the components of the tensor R_{ij} discussed in Sec. III A. Note that knowledge of Q_{ij} and R_{ij} allows one to construct easily the tensor analogous to R_{ij}, but for electrons. This might be useful for the analysis of deformations of electron density distribution in a cluster.

The quadrupole moment tensor can be expressed via the tensor $\tilde{Q}_{ij} = \langle \Sigma q x_i x_j \rangle$ characterizing the average dimensions of the total charge distribution. Here, the angular brackets mean averaging over the electronic charge distribution. The principal values of the tensor $\tilde{Q}_{ij}$ should be negative at least for neutral clusters, because electron density is spilled out of the cluster, which makes its distribution a little broader than the distribution of ions. A similar situation occurs for cluster ions, but in this case there is a noncompensated positive charge in the system, which brings a certain positive contribution to $\tilde{Q}_{ij}$ and makes the principal values of $\tilde{Q}_{ij}$ positive in some cases.

The numerical analysis performed in this work shows that for neutral sodium clusters the principal values of $\tilde{Q}_{ij}$ are

always negative, while for the small cluster ions Na_2^+, Na_3^+, and Na_4^+ (C_{2v}) some of the principal values are positive.

The principle values of the quadrupole moment tensor characterize the distortion of the total cluster charge distribution. Indeed, Fig. 12 shows that the Na_8 and Na_{20} tetrahedral group isomers have zero quadrupole moments, which reflect the closeness to sphericity of the magic clusters. Our calculations demonstrate that for some open shell clusters like Na_{11} and Na_{12} the quadrupole moments turn out to be rather small, although the ionic charge distribution in these clusters has a prominent deformation as is clear from Figs. 1 and 5. The small quadrupole moments in these clusters are the result of compensation of the electron and ion components of Q_{ij}.

The quadrupole moment diagram allows one to make some conclusions about the type of shape of the total charge distribution in a cluster. The average dimensions of the cluster total charge distribution in the *x*, *y*, and *z* directions can be characterized by the quantities $Q_z^{\|}=\tilde{Q}_{zz}=\langle \Sigma ez^2\rangle$, $Q_x^{\perp}=\tilde{Q}_{xx}=\langle \Sigma ex^2\rangle$, and $Q_y^{\perp}=\tilde{Q}_{yy}=\langle \Sigma ey^2\rangle$. Here, the summation is performed over all electrons and ions in the cluster and the angular brackets mean averaging. These quantities are connected with the quadrupole moments tensor defined in Eq. (21). Indeed, in both the prolate and oblate cases, when $Q_x^{\perp}=Q_y^{\perp}=Q^{\perp}$ and $Q_z^{\|}=Q^{\|}$, the principal values of the tensor Q_{ij} read

$$Q_{zz}=2(Q^{\|}-Q^{\perp}),$$

$$Q_{xx}=(Q^{\perp}-Q^{\|})=-\frac{Q_{zz}}{2},$$

$$Q_{yy}=Q_{xx}=-\frac{Q_{zz}}{2}. \tag{22}$$

These equations define the important relationships between the principal values of the quadrupole moment tensor in the oblate and prolate cases and help understand the quadrupole moments diagrams shown in Figs. 12 and 13.

Equations (22) show that the sign of the principal values Q_{xx}, Q_{yy}, and Q_{zz} depends on the relative values of $Q^{\|}$ and $Q^{\perp}$. With the use of Eqs. (22) and the cluster quadrupole moment diagrams shown in Figs. 12 and 13, one can easily analyze the total charge distribution of the clusters shown in Figs. 1 and 2. Note that conclusions made about the shape of the total charge distribution and the shape of the ionic component (see Figs. 5 and 6) sometimes differ significantly one from another for some clusters. For example, the ionic charge distribution in the Na_{12} cluster has a prolate shape, while the total charge distribution is oblate.

The quadrupole moments of singly charged sodium clusters differ substantially from those for the corresponding neutral ones. The excess positive charge leads to the rearrangement of the cluster structure and to the appearance of a quadrupole moment in cluster ions like Na_8^+ and Na_{20}^+. Although the electron exchange-correlation force in a cluster turns out to be insufficient to change the cluster geometry significantly enough to make a magic cluster ion Na_9^+, having a closed shell electronic structure of delocalized electrons, spherical-like without a quadrupole moment. Instead, Na_9^+ retains a noticeable deformation.

Let us now discuss an idea for which the cluster multipole moments play a crucial role and consider the possibility of cluster isomer separation by placing the mass selected cluster beam in an inhomogeneous external field. As we have seen from the calculations presented above, different cluster isomers of the same mass often possess different structure and as a result of that different multipole moments (dipole or quadrupole). However, such cluster isomers are indistinguishable in experiments nowadays with mass selected cluster beams. They can nevertheless be separated if one puts the mass selected cluster beam in an inhomogeneous external field. Let us estimate this effect for the characteristic values of the dipole and quadrupole moments calculated above.

From the dipole moment diagrams shown in Figs. 10 and 11 one can conclude that the difference in dipole moments for some cluster isomers can be as large as 1 D and for the quadrupole often it is about 40 D Å or even larger. The force acting on a cluster with the dipole moment **D** in an external inhomogeneous electric field $\mathbf{E}(\mathbf{r})$ is equal to [65]

$$\mathbf{F}^D(\mathbf{r})=\boldsymbol{\nabla}\{\mathbf{D}\cdot\mathbf{E}(\mathbf{r})\}. \tag{23}$$

The component of the force acting on the cluster with quadrupole moment Q_{ij} is as follows [65]:

$$F_i^Q(\mathbf{r})=\boldsymbol{\nabla}_i\left\{\frac{Q_{jk}}{6}\boldsymbol{\nabla}_j E_k(\mathbf{r})\right\}. \tag{24}$$

Here, summation is assumed over the repeated indices *j* and *k* of the vector and tensor components in the right hand side of Eq. (24).

Let us introduce the time period τ during which the cluster beam passes through the inhomogeneous electric field. One can estimate the distance Δ by which isomers will be separated during this period of time as $\Delta\sim F\tau^2/2M$, where *M* is the mass of the isomer considered and *F* is the force acting on either the dipole [see Eq. (23)] or quadrupole [see Eq. (24)] moment of the cluster. Substituting in these equations the characteristic values for the dipole and quadrupole moments, assuming that the inhomogeneity of the electric field is about $\boldsymbol{\nabla}E\sim 5\times 10^3$ V/cm^2, one derives from Eqs. (23) and (24) that during the period $\tau\sim 10^{-3}$ s the isomers with $N=3$ and $\delta D\sim 1$ D become separated by $\Delta\sim 0.7$ mm and that $\Delta\sim 2.8$ mm for $\delta Q\sim 40$ D Å, $\tau\sim 10$ s, $N=5$, and no dipole moment.

These estimates demonstrate that one can create significant separation distances for reasonably short periods of time with the electric field strengths and their gradients achievable in laboratory conditions. Experiments with mass selected and isomer separated cluster beams might provide the most accurate information on the structure and properties of atomic clusters.

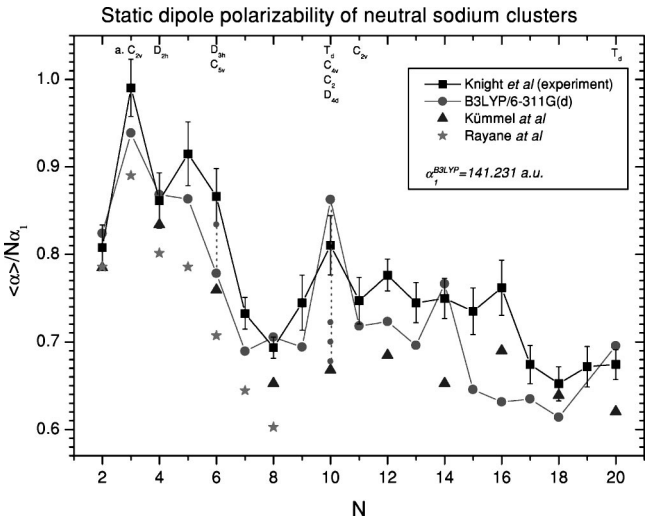

FIG. 14. Static mean polarizability per atom for neutral sodium clusters normalized to the polarizability of a single sodium atom. Circles show the results derived in this work by the B3LYP method. For some clusters, more than one isomer has been considered. In these cases, labels indicate the point symmetry group of corresponding isomers. Stars and triangles represent the polarizabilities calculated in [19] and [32], respectively. Squares are the experimental values taken from [21].

E. Polarizabilities

We have calculated the polarizabilities for the optimized neutral sodium clusters (see Fig. 1) as a function of cluster size. Results of this calculation are shown in Fig. 14. In this figure, we also plot experimental points from [21]. Calculation of the polarizabilities was performed by the B3LYP method. Figure 14 demonstrates quite reasonable agreement of the B3LYP results with the experimental data.

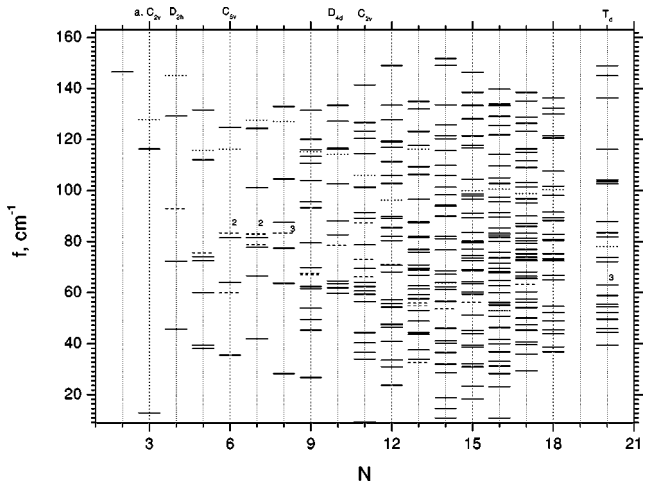

FIG. 15. Normal vibration frequencies calculated by the B3LYP method for the neutral sodium clusters with $N \leqslant 20$. For each cluster we mark the breathing mode in the spectrum by dotted line and the surface quadrupole vibration modes by dashed lines. The number near some of the lines indicate the degeneracy of the corresponding quadrupole surface vibration mode.

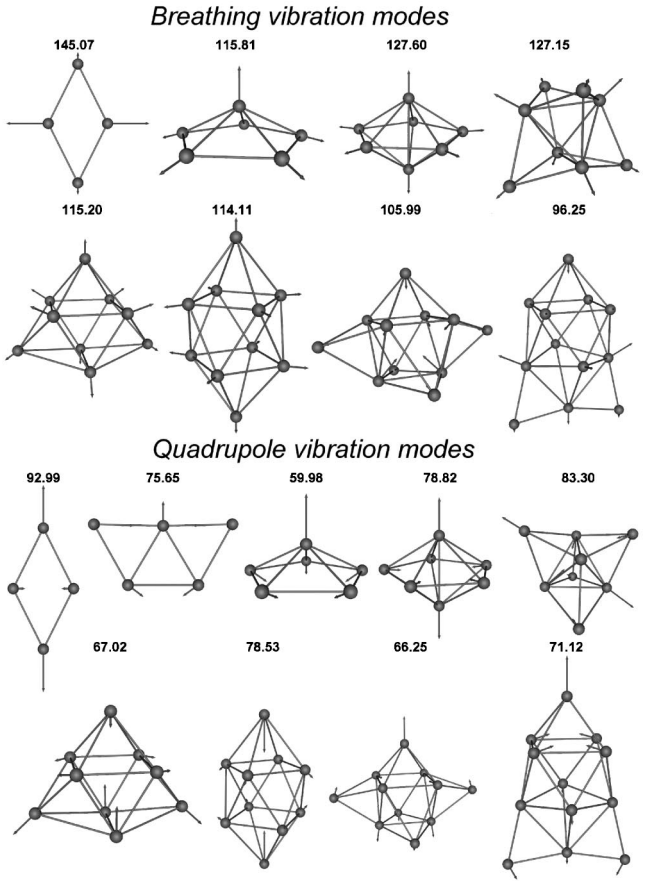

FIG. 16. Surface and volume vibration modes for the selected neutral sodium clusters. Number near each cluster image indicates the frequency of the corresponding normal vibration mode. The values are given in cm^{-1}.

In Fig. 14 we also compare the polarizabilities calculated in our work with those derived by other theoretical methods [19,32]. This figure demonstrates a satisfactory agreement of the results of different approaches with each other and with the experimental data. This comparison is quite important, because in our work as well as in [19] the polarizabilities have been calculated using an all-electron *ab initio* approach, while in [32] they were obtained with the use of pseudopotentials. Note that our points are closer to the experimental values than those from [19], in spite of the fact that both calculations have been performed on the basis of density functional theory. The differences between the two schemes of calculation arise in the form of the density functional and the set of basis functions employed. In [19], the so-called Perdew-Wang 91 density functional (see, e.g., [62] and references therein) was used, while we applied its B3LYP form.

Let us also compare the polarizabilities for the Na_8 and Na_{20} clusters calculated in the random phase approximation with exchange in the spherical jellium model ($\alpha_{Na_8} = 755$ a.u. and $\alpha_{Na_{20}} = 1808$ a.u. [66]) with our results ($\alpha_{Na_8} = 797$ a.u. and $\alpha_{Na_{20}} = 1964$ a.u.). The closeness of the values shows that the detailed ionic core structure does not much influence the values of the cluster polarizabilities.

This comparison shows that the jellium model turns out to be quite a reasonable approximation.

Figure 14 shows that the disagreement between theoretical and experimental points is not always less than the experimental error bars. This disagreement might indicate that for certain N cluster isomers have been experimentally detected other than those calculated in our work. For example, the calculated value $\alpha_{Na_6}^{C_{5v}}=659$ a.u. lies beyond the experimental error bars, while $\alpha_{Na_6}^{D_{3h}}=706.876$ a.u. is within the range of the experimental error.

Note that the polarizabilities of the clusters Na_8, Na_{10}, and Na_{20}, possessing the T_d point symmetry group, surpass the corresponding experimental values a little, although being quite close to them. For the Na_8 and Na_{10} clusters, the disagreement of the theoretical and experimental values is within the range of the experimental error.

A similar situation occurs for the Na_{14} cluster, characterized by the C_{2v} point symmetry group. This cluster likely belongs to the cluster chain leading to the formation of the tetrahedral Na_{20} cluster from the tetrahedral Na_8 (see our discussion in Sec. III A). This situation allows us to assume that the polarizabilities of other clusters of this chain, which we have not analyzed in this paper because they are energetically not favorable, will also be quite close to the experimental values.

F. Normal vibration modes

Using the B3LYP method, we have calculated the normal vibration frequencies for the optimized neutral sodium clusters. The results of this calculation are shown in Fig. 15. In this figure, we indicate the point symmetry group for those clusters for which more than one cluster isomer has been considered (see Fig. 1). Numerous frequencies shown in Fig. 15 are degenerate or nearly degenerate. This explains why the total number of frequencies for most clusters is less than the number of vibrational degrees of freedom available in the system. In the more symmetric clusters, like Na_7, Na_8, Na_{10}, or Na_{20}, the rate of degeneracy of the normal vibration modes is higher.

Knowledge of the normal vibration modes and their frequencies is important for a physical understanding and quantitative description of the relaxation of electron plasmon excitations in metal clusters [42]. One can visualize normal vibration modes, showing the directions and amplitudes of the atom displacements by corresponding vectors. Since it is difficult to show all such pictures in this paper due to their large number, we focus instead only on the two types of breathing modes and quadrupole surface vibration modes. These modes were considered in [42] within the dynamical jellium model [41] for the treatment of electron-phonon coupling in the spherical metal clusters Na_{20}, Na_{40}, and Na_{92}.

In this paper, we discuss the appearance of these specific vibration modes in a cluster system and compare their frequencies with the predictions made in [42] on the basis of the jellium model. For this purpose, we have analyzed all calculated vibration modes and identified the breathing and quadrupole vibrations for each cluster. In Fig. 16, we present images of the breathing and quadrupole vibration modes for some clusters to illustrate how the identification of the modes has been performed.

The results of this analysis are shown in Fig. 15, where for each cluster we mark the breathing mode in the spectrum by dotted lines and the surface quadrupole vibration modes by dashed lines. The number near some of the lines indicate the degeneracy of the corresponding quadrupole surface vibration mode. The degeneracy rate and the number of quadrupole surface vibration modes can easily be understood with the help of the cluster images shown in Fig. 1. This figure shows that the prototype of the breathing mode exists already in the Na_3 and Na_4 clusters. For the Na_4 cluster, one can identify the quadrupole surface vibration mode, although it is meaningful to discuss surface vibrations only for the Na_6 cluster and larger. Figure 15 shows that the frequencies of the breathing and surface vibration modes decrease systematically with increasing cluster size, although this decrease has numerous irregularities, particularly for the clusters with $N<8$. The frequency of the breathing mode decreases faster with the growth of N than the frequency of the quadrupole surface vibration mode.

Let us compare the calculated frequencies of the breathing and surface vibration modes with the predictions of the jellium model. In [42], it was shown that the breathing vibration mode frequencies calculated for the spherical Na_{20}, Na_{40}, and Na_{92} within the framework of the dynamical jellium model are quite close to the values derived from the phonon dispersion law for metals [67]

$$\Omega^2=\frac{3v_F^2k^2}{M_{Na}(9+k^2v_F^2r_0^3)}, \tag{25}$$

where $M_{Na}=4.2\times10^4$ is the mass of the sodium atom, $v_F=(9\pi/4)^{1/3}/r_0$ is the velocity of cluster electrons on the Fermi surface, and r_0 is the Wigner-Seitz radius. In the long wave limit, Eq. (25) reduces to the Bohm-Staver formula for the velocity of sound, $d\Omega/dk=v_F/\sqrt{3M_{Na}}\approx3\times10^5$ cm/s. This number is quite close to the real value of the velocity of sound in bulk sodium: 3.2×10^5 cm/s.

Using the dispersion law (25), we estimate the breathing mode frequencies for the magic Na_8 and Na_{20} clusters. The results of this calculation are as follows: $\Omega_{Na_8}=104.09$ cm^{-1}, $\Omega_{Na_{20}}=80.49$ cm^{-1}. In this calculation we used $r_0=4$.

The frequency values obtained from Eq. (25) are close to those presented in Fig. 15, $\Omega_{Na_8}=127.15$ cm^{-1}, $\Omega_{Na_{20}}=78.11$ cm^{-1}. The agreement of the frequencies is rather good for the Na_{20} cluster. For Na_8, the agreement is reasonable, but not as good as for Na_{20}. Some disagreement arises due to the fact that the Wigner-Seitz radius for the Na_8 cluster is about 10% smaller than its bulk value. Indeed, substituting $r_0=3.6$ in Eq. (25) one derives $\Omega_{Na_8}=127.10$ cm^{-1}, which is in nearly perfect agreement with the *ab initio* result. The decrease of the Wigner-Seitz radius can be easily understood from analysis of the cluster geometry shown in Fig. 1.

Now let us compare the quadrupole surface vibration mode frequencies calculated here (see Fig. 15) with those following from the dynamical jellium model. According to [42], the quadrupole surface vibration frequencies Ω_2 for the spherical Na_{20}, Na_{40}, and Na_{92} clusters are equal to 56.48 cm^{-1}, 48.41 cm^{-1}, and 32.28 cm^{-1}, respectively. The value of the quadrupole surface vibration frequency for the Na_{20} cluster calculated in the present work is equal to 63.15 cm^{-1}, which is rather close to the value predicted in [42].

The values of the quadrupole surface vibration frequencies calculated for Na_{20}, Na_{40}, and Na_{92} show relatively slow decrease with growth in cluster size. Extrapolating these values toward smaller cluster sizes, we derive frequency values that are consistent with those shown in Fig. 15. This comparison demonstrates that the jellium model calculation of the surface vibration frequencies is in reasonable agreement with the more accurate *ab initio* many-body theory.

The comparison of the jellium model results with those derived by the more accurate *ab initio* many-body theory is important, because it forms the theoretical background for the jellium model calculations in larger cluster systems, for which *ab initio* methods are hardly possible. The comparison with the jellium model that we performed in this paper can be extended toward larger cluster sizes and other collective modes of ion motion.

IV. CONCLUSION

In this paper we have calculated the optimized structure and various characteristics of sodium clusters consisting of up to 20 atoms. We have used three different methods: B3LYP, MP_4 and HF. It was demonstrated that the first two methods, because they account for many-electron correlations, provide much better agreement with the available experimental data and theoretical results based on the configuration-interaction method as compared to that for the Hartree-Fock approximation. This was checked for various cluster characteristics: cluster geometries, binding energies per atom, and ionization potentials.

We have also calculated and analyzed the dependence of the ionic and total quadrupole moments of sodium clusters as a function of their size. It was demonstrated that the cluster shapes characterized by the quadrupole moments are in reasonable agreement with the predictions of the jellium model and the results of experimental observations.

We have determined the normal vibration modes and their frequencies for a number of clusters and demonstrated their qualitative agreement with the predictions based on the jellium model.

The results of this work can be extended in various directions. One can use similar methods to study the structure and properties of various types of cluster. It would be interesting to extend the calculations toward larger cluster sizes and perform more comparisons with the results following from the jellium model and other simplified theories, based either on pseudopotentials or effective interatomic potentials. Many interesting problems arise when considering collisions and electron excitations in clusters with optimized geometries. These and many more other problems in atomic cluster physics can be tackled with the use of the methods considered in our work.

ACKNOWLEDGMENTS

The authors acknowledge support from the INTAS, the Volkswagen Foundation, the Alexander von Humboldt Foundation, and DAAD.

APPENDIX: TABLES

In this appendix, we present tables of the essential cluster characteristics. The binding energies per atom for neutral and singly charged clusters are compiled in Tables I and II. The principal values of the quadrupole moment tensors for neutral and singly charged clusters are presented in Tables III and IV.

TABLE I. Total energies of the optimized neutral sodium clusters. Numbers of atoms in clusters are given in the first column. In the second column, the point symmetry groups of the clusters are shown. In the next three columns, the cluster total energies derived by the HF, MP_4, and B3LYP methods are compiled. For the sake of comparison, the total energies computed by the CI method in [16] are presented in the sixth column.

		E_N(a.u.)			
N	Symmetry	HF/6-311G(d)	MP4/6-311G(d,p)	B3LYP/6-311G(d)	Reference [16]
1		−161.8459	−161.8459	−162.2866	
2	$D_{\infty h}$	−323.6911	−323.7149	−324.5999	−323.3176
3	$D_{\infty h}$	−485.5405	−485.5626	−486.8963	
	${}_{a.}C_{2v}$	−485.5403	−485.5653	−486.8960	−484.9729
	${}_{b.}C_{2v}$	−485.5385	−485.5656	−486.8939	
	D_{3h}	−485.5282	−485.5626	−486.8889	
4	D_{2h}	−647.3871	−647.4433	−649.2076	−646.6494
	D_{4h}	−647.3897		−649.1965	
5	C_{2v}	−809.2518	−809.3008	−811.5164	−808.3174

TABLE I. (*Continued*).

		E_N(a.u.)			
N	Symmetry	HF/6-311G(d)	MP4/6-311G(d,p)	B3LYP/6-311G(d)	Reference [16]
6	C_{5v}	−971.0915	−971.1880	−973.8324	−969.9899
	D_{3h}	−971.0998	−971.1872	−973.8344	−989.9884
7	D_{5h}	−1132.9462	−1133.0634	−1136.1430	−1131.6610
8	T_d	−1294.8015	−1294.9410	−1298.4606	−1293.3395
9	C_{2v}	−1456.6466		−1460.7597	
10	C_2			−1623.0758	
	D_{4d}			−1623.0734	
	C_{4v}			−1623.0554	
	T_d			−1623.0530	
11	C_{2v}			−1785.3737	
	C_1			−1785.3726	
12	C_{2v}			−1947.6917	
13	C_1			−2110.0045	
14	C_{2v}			−2272.3092	
15	C_s			−2434.6188	
16	C_s			−2596.9370	
17	C_s			−2759.2537	
18	C_{5v}			−2921.5704	
19	D_{5h}			−3083.8730	
20	T_d			−3246.2015	
	C_{2v}			−3246.1981	

TABLE II. Total energies of the optimized singly charged sodium clusters. Numbers of atoms in clusters are given in the first column. In the second column, the point symmetry groups of the clusters are shown. In the next three columns, the cluster total energies derived by the HF, MP_4, and B3LYP methods are compiled.

		E_N^+ (a.u.)		
N	Symmetry	HF/6-311G(d)	MP4/6-311G(d,p)	B3LYP/6-311G(d)
1		−161.6642	−161.6642	−162.0874
2	$D_{\infty h}$	−323.5447	−323.5447	−324.4114
3	D_{3h}	−485.4084	−485.4322	−486.7457
4	D_{2h}	−647.2653	−647.2915	−649.0502
	C_{2v}	−647.2681	−647.2919	−649.0489
5	D_{2h}	−809.1226	−809.1740	−811.3727
	D_{2d}			−811.3629
6	C_{2v}	−970.9749	−971.0364	−973.6742
7	D_{5h}	−1132.8278	−1132.9261	−1135.9994
8	C_{2v}	−1294.6866	−1294.7863	−1298.3082
9	D_{3h}	−1456.5346		−1460.6326
10	D_{4d}			−1622.9335
	C_{4v}			−1622.9278
	T_d			−1622.9273
11	D_{3h}			−1785.2509
	C_s			−1785.2455
12	C_{2v}			−1947.5479
13	C_1			−2109.8718
14	C_{2v}			−2272.1654
15	C_s			−2434.4907
16	C_s			−2596.8051
17	C_s			−2759.1222
18	C_s			−2921.4365
19	D_{5h}			−3083.7499
20	C_{2v}			−3246.0655
21	O_h			−3408.3434

TABLE III. Principal values of the quadrupole moment tensor calculated for neutral sodium clusters. The first column shows numbers of atoms in clusters. The second column gives their point symmetry groups. In the last three columns, the principal values Q_{xx}, Q_{yy}, and Q_{zz} are given. They have been computed by the B3LYP method.

N	Symmetry	Q_{xx} (D Å)	Q_{yy} (D Å)	Q_{zz} (D Å)
2	$D_{\infty h}$	−11.5622	−11.5622	23.1244
3	${}_{a.}C_{2v}$	−9.9300	−5.3883	15.3183
	${}_{b.}C_{2v}$	−7.5625	31.0631	−23.5006
	$D_{\infty h}$	−16.3309	−16.3309	32.6618
4	D_{2h}	−12.9139	26.2865	−13.3726
	D_{4h}	5.1177	5.1177	−10.2354
5	C_{2v}	−20.3760	23.0544	−2.6784
6	C_{5v}	6.5817	6.5817	−13.1634
	D_{3h}	14.4807	14.4807	−28.9614
7	D_{5h}	13.3285	13.3285	−26.6570
8	T_d	0.0000	0.0000	0.0000
9	C_{2v}	−22.2202	−7.8457	30.0659
10	D_{4d}	13.5248	13.5248	−27.0496
	C_2	31.6087	−15.5561	−16.0526
	C_{4v}	−14.6949	−14.6949	29.3898
	T_d	0.0000	0.0000	0.0000
11	C_{2v}	−0.3816	3.6348	−3.2532
	C_1	−18.4455	13.9570	4.48848
12	C_{2v}	0.0392	1.7777	−1.8169
13	C_1	3.5616	7.3169	−10.8785
14	C_{2v}	−40.2978	54.2376	−13.9398
15	C_s	−9.0476	−21.7878	30.8354
16	C_s	−18.0272	1.6718	16.3554
17	C_s	2.2310	18.9437	−21.1747
18	C_{5v}	−14.0456	−14.0540	28.0996
19	D_{5h}	−2.9626	−2.9626	5.9252
20	T_d	0.0000	0.0000	0.0000
	C_{2v}	−69.7510	79.8143	−10.0633

TABLE IV. Principal values of the quadrupole moment tensor calculated for singly charged sodium clusters. The first column shows numbers of atoms in clusters. The second column gives their point symmetry groups. In the last three columns, the principal values Q_{xx}, Q_{yy}, and Q_{zz} are given. They have been computed by the B3LYP method.

N	Symmetry	Q_{xx} (D Å)	Q_{yy} (D Å)	Q_{zz} (D Å)
2	$D_{\infty h}$	−27.9109	−27.9109	55.8218
3	D_{3h}	21.8547	21.8547	−43.7094
4	D_{2h}	−67.8170	−12.6716	80.4886
	C_{2v}	−86.4460	−27.4786	113.9246
5	D_{2h}	−101.2157	6.2746	94.9411
	D_{2d}	−46.6091	−46.6091	93.2182
6	C_{2v}	−34.9108	53.8712	−18.9604
7	D_{5h}	24.3267	24.3267	−48.6534
8	C_{2v}	4.4346	−51.8751	47.4405
9	D_{3h}	23.1994	23.1994	−46.3988
10	D_{4d}	−34.9547	−34.9547	69.9094
	C_{4v}	−3.5448	−3.5448	7.0896
	T_d	0.0000	0.0000	0.0000
11	D_{3h}	−18.5476	−18.5476	37.0952
	C_s	19.4836	−10.0197	−9.46382
12	C_{2v}	−58.0823	−21.8996	79.9819
13	C_1	69.5400	25.4745	−95.0145
14	C_{2v}	−178.1183	149.0275	29.0908
15	C_s	−37.4527	44.8752	−7.4225
16	C_s	−55.6664	58.5058	−2.8394
17	C_s	−47.1267	60.3728	−13.2461
18	C_s	−33.5207	65.9999	−32.4792
19	D_{5h}	−57.3045	−57.3045	114.6090
20	C_{2v}	−79.3111	95.8676	−16.5565
21	O_h	0.0967	0.0967	−0.1934

[1] W. D. Knight, K. Clemenger, W. A. de Heer, W. A. Saunders, M. Y. Chou, and M. L. Cohen, Phys. Rev. Lett. **52**, 2141 (1984).

[2] C. Bréchignac, Ph. Cahuzac, F. Carlier, and J. Leygnier, Chem. Phys. Lett. **164**, 433 (1989).

[3] K. Selby, M. Vollmer, J. Masui, V. Kresin, W. A. de Heer, and W. D. Knight, Phys. Rev. B **40**, 5417 (1989).

[4] K. Selby, V. Kresin, J. Masui, M. Vollmer, W. A. de Heer, A. Scheidemann, and W. D. Knight, Phys. Rev. B **43**, 4565 (1991).

[5] G. F. Bertsch, A. Bulgac, D. Tomanek, and Y. Wang, Phys. Rev. Lett. **67**, 2690 (1992).

[6] I. V. Hertel, H. Steger, J. de Vries, B. Weisser, C. Menzel, B. Kamke, and W. Kamke, Phys. Rev. Lett. **68**, 784 (1992).

[7] A. Herlert, S. Krückeberg, L. Schweikhard, M. Vogel, and C. Walther, Phys. Scri. T **80**, 200 (1999).

[8] W. A. de Heer, Rev. Mod. Phys. **65**, 611 (1993).

[9] M. Brack, Rev. Mod. Phys. **65**, 677 (1993).

[10] C. Bréchignac and J. P. Connerade, J. Phys. B **27**, 3795 (1994).

[11] *Clusters of Atoms and Molecules, Theory, Experiment and Clusters of Atoms*, edited by H. Haberland, Springer Series in Chemical Physics Vol. 52 (Springer, Berlin, 1994).

[12] U. Näher, S. Bjørnholm, S. Frauendorf, F. Garcias, and C. Guet, Phys. Rep. **285**, 245 (1997).

[13] *Metal Clusters*, edited by W. Ekardt (Wiley, New York, 1999).

[14] *Atomic Clusters and Nanoparticles*, NATO Advanced Study Institute, Les Houches Session LXXIII, Les Houches, 2000, edited by C. Guet, P. Hobza, F. Spiegelman and F. David (EDP Sciences and Springer Verlag, Berlin, 2001).

[15] I. Boustani, W. Pewestorf, P. Fantucci, V. Bonačić-Koutecký,

and J. Koutecký, Phys. Rev. B **35**, 9437 (1987).
[16] V. Bonačić-Koutecký, P. Fantucci, and J. Koutecký, Phys. Rev. B **37**, 4369 (1988).
[17] I. Boustani and J. Koteckýy, J. Chem. Phys. **88**, 5657 (1988).
[18] V. Bonačić-Koteckýy, I. Boustani, M. F. Guest, and J. Koteckýy, J. Chem. Phys. **89**, 4861 (1988).
[19] D. Rayane *et al.*, Eur. Phys. J. D **9**, 243 (1999).
[20] H. Akeby, I. Panas, L. G. M. Petterson, P. Siegbahn, and U. Wahlgreen, J. Chem. Phys. **94**, 5471 (1990).
[21] W. D. Knight, K. Clemenger, W. A. de Heer, and W. A. Saunders, Phys. Rev. B **31**, 2539 (1985).
[22] C. Bréchignac, Ph. Cahuzac, J. Leygnier, and J. Weiner, J. Chem. Phys. **90**, 1492 (1989).
[23] C. Bréchignac, Ph. Cahuzac, F. Carlier, M. de Frutos, and J. Leygnier, J. Chem. Phys. **93**, 7449 (1990).
[24] C. Bréchignac, Ph. Cahuzac, F. Carlier, J. Leygnier, and A. Sarfati, Phys. Rev. B **44**, 11 386 (1991).
[25] W. A. de Heer, K. Selby, V. Kresin, J. Masui, M. Vollmer, A. Chatelain, and W. D. Knight, Phys. Rev. Lett. **59**, 1805 (1987).
[26] J. L. Martins, J. Buttet, and R. Car, Phys. Rev. B **31**, 1804 (1985).
[27] F. Spiegelmann, R. Poteau, B. Montag, and P.-G. Reinhard, Phys. Lett. A **242**, 163 (1998).
[28] F. Nogueira, J. L. Martins, and C. Fiolhais, Eur. Phys. J. D **9**, 229 (1999).
[29] R. Gutiérrez, F. Grossmann, O. Knospe, and R. Schmidt, Phys. Rev. A **64**, 013202 (2001).
[30] S. A. Blundell, C. Guet, and Rajendra R. Zope, Phys. Rev. Lett. **84**, 4826 (2000).
[31] L. Kronik, I. Vasiliev, and J. R. Chelikowsky, Phys. Rev. B **62**, 9992 (2000).
[32] S. Kümmel, T. Berkus, P.-G. Reinhard, and M. Brack, Eur. Phys. J. D **11**, 239 (2000).
[33] S. Kümmel, J. Akola, and M. Manninen, Phys. Rev. Lett. **84**, 3827 (2000).
[34] J. L. Martins, R. Car, and J. Buttet, Surf. Sci. **106**, 265 (1981).
[35] A. Hintermann and M. Manninen, Phys. Rev. B **27**, 7262 (1983).
[36] W. Ekardt, Phys. Rev. B **29**, 1558 (1984).
[37] W. Ekardt, Phys. Rev. B **32**, 1961 (1985).
[38] C. Guet and W. R. Johnson, Phys. Rev. B **45**, 11 283 (1992).
[39] V. K. Ivanov, A. N. Ipatov, V. A. Kharchenko, and M. L. Zhizhin, Pis'ma Zh. Eksp. Teor. Fiz. **58**, 649 (1993); Phys. Rev. A **50**, 1459 (1994).
[40] A. G. Lyalin, S. K. Semenov, A. V. Solov'yov, N. A. Cherepkov, and W. Greiner, J. Phys. B **33**, 3653 (2000).
[41] L. G. Gerchikov, A. V. Solov'yov, and W. Greiner, Int. J. Mod. Phys. E **8**, 289 (1999).
[42] L. G. Gerchikov, A. N. Ipatov, A. V. Solov'yov, and W. Greiner, J. Phys. B **33**, 4905 (2000).
[43] V. K. Ivanov, in *Correlations in Clusters and Related Systems*, edited by J.-P. Connerade (World Scientific, Singapore, 1996), pp. 73–91.
[44] G. F. Bertsch, A. Bulgac, D. Tomanek, and Y. Wang, Phys. Rev. Lett. **67**, 2690 (1991).
[45] V. K. Ivanov, G. Yu. Kashenock, R. G. Polozkov, and A. V. Solov'yov, J. Phys. B (to be published).
[46] L. G. Gerchikov, J. P. Connerade, A. V. Solov'yov, and W. Greiner, J. Phys. B **30**, 4133 (1997).
[47] L. G. Gerchikov, P. V. Efimov, V. M. Mikoushkin, and A. V. Solov'yov, Phys. Rev. Lett. **81**, 2707 (1998).
[48] L. G. Gerchikov, A. N. Ipatov, and A. V. Solov'yov, J. Phys. B **30**, 5939 (1997).
[49] L. G. Gerchikov, A. N. Ipatov, A. V. Solov'yov, and W. Greiner, J. Phys. B **31**, 3065 (1998).
[50] L. G. Gerchikov, A. N. Ipatov, R. G. Polozkov, and A. V. Solov'yov, Phys. Rev. A **62**, 043201 (2000).
[51] J. P. Connerade, L. G. Gerchikov, A. N. Ipatov, and A. V. Solov'yov, J. Phys. B **31**, L27 (1998).
[52] J. P. Connerade, L. G. Gerchikov, A. N. Ipatov, and A. V. Solov'yov, J. Phys. B **32**, 877 (1999).
[53] L. G. Gerchikov and A. V. Solov'yov, Z. Phys. D: At., Mol. Clusters **42**, 279 (1997).
[54] L. G. Gerchikov, A. N. Ipatov, and A. V. Solov'yov, J. Phys. B **31**, 2331 (1998).
[55] A. V. Solov'yov, in *Atomic Clusters and Nanoparticles* (Ref. [14]).
[56] M. J. Frisch *et al.*, computer code GAUSSIAN 98, Rev. A. 9, Gaussian Inc., Pittsburgh, PA, 1998.
[57] L. Lindgren and J. Morrison, *Atomic Many-Body Theory* (Springer, New York, 1986).
[58] James B. Foresman and Æeleen Frisch, *Exploring Chemistry with Electronic Structure Methods* (Gaussian Inc., Pittsburgh, PA, 1996).
[59] C. Møller and M. S. Plesset, Phys. Rev. **46**, 618 (1934).
[60] L. D. Landau and E. M. Lifshitz, *Quantum Mechanics* (Pergamon, London, 1965).
[61] A. D. Becke, Phys. Rev. A **38**, 3098 (1988).
[62] K. Burke, J. P. Perdew, and Y. Wang, in *Electronic Density Functional Theory: Recent Progress and New Directions*, edited by J. F. Dobson, G. Vignale, and M. Das (Plenum, New York, 1998).
[63] C. Lee, W. Yang, and R. G. Parr, Phys. Rev. B **37**, 785 (1988).
[64] S. H. Vosko, L. Wilk, and M. Nusair, Can. J. Phys. **58**, 1200 (1980).
[65] L. D. Landau and E. M. Lifshitz, *The Classical Theory of Fields* (Pergamon, London, 1959).
[66] M. Madjet, C. Guet, and W. R. Johnson, Phys. Rev. A **51**, 1327 (1995).
[67] C. Kittel, *Introduction to Solid State Physics* (Wiley, London, 1967).
[68] D. Salahub, in *Atomic Clusters and Nanoparticles* (Ref. [14]).